Physics Reports 528 (2013) 47–89

Contents lists available at SciVerse ScienceDirect

Physics Reports

journal homepage: www.elsevier.com/locate/physrep

Rogue waves and their generating mechanisms in different physical contexts

M. Onorato [a,b], S. Residori [c,*], U. Bortolozzo [c], A. Montina [d], F.T. Arecchi [e,f]

[a] Dipartimento di Fisica Generale, Università degli Studi di Torino, Via Pietro Giuria 1, 10125 Torino, Italy
[b] INFN, Sezione di Torino, Via Pietro Giuria 1, 10125 Torino, Italy
[c] INLN, Université de Nice Sophia-Antipolis, CNRS, 1361 route des Lucioles, 06560 Valbonne, France
[d] Perimeter Institute for Theoretical Physics, Waterloo, Ontario, N2L 2Y5 Canada
[e] Dipartimento di Fisica, Università di Firenze, Italy
[f] CNR-INO, largo E. Fermi 6, 50125 Firenze, Italy

ARTICLE INFO

Article history:
Accepted 19 December 2012
Available online 14 March 2013
editor: G.I. Stegeman

ABSTRACT

Rogue waves is the name given by oceanographers to isolated large amplitude waves, that occur more frequently than expected for normal, Gaussian distributed, statistical events. Rogue waves are ubiquitous in nature and appear in a variety of different contexts. Besides water waves, they have been recently reported in liquid Helium, in nonlinear optics, microwave cavities, etc. The first part of the review is dedicated to rogue waves in the oceans and to their laboratory counterpart with experiments performed in water basins. Most of the work and interpretation of the experimental results will be based on the nonlinear Schrödinger equation, an universal model, that rules the dynamics of weakly nonlinear, narrow band surface gravity waves. Then, we present examples of rogue waves occurring in different physical contexts and we discuss the related anomalous statistics of the wave amplitude, which deviates from the Gaussian behavior that were expected for random waves. The third part of the review is dedicated to optical rogue waves, with examples taken from the supercontinuum generation in photonic crystal fibers, laser fiber systems and two-dimensional spatiotemporal systems. In particular, the extreme waves observed in a two-dimensional spatially extended optical cavity allow us to introduce a description based on two essential conditions for the generation of rogue waves: nonlinear coupling and nonlocal coupling. The first requirement is needed in order to introduce an elementary size, such as that of the solitons or breathers, whereas the second requirement implies inhomogeneity, a mechanism needed to produce the events of mutual collisions and mutual amplification between the elementary solitons or wavepackets. The concepts of "granularity" and "inhomogeneity" as joint generators of optical rogue waves are introduced on the basis of a linear experiment. By extending these concepts to other systems, rogue waves can be classified as phenomena occurring in the presence of many uncorrelated "grains" of activity inhomogeneously distributed in large spatial domains, the "grains" being of linear or nonlinear origin, as in the case of wavepackets or solitons.

Contents

* Corresponding author. Tel.: +33 0492967317.
E-mail address: Stefania.Residori@inln.cnrs.fr (S. Residori).

0370-1573/$ – see front matter © 2013 Elsevier B.V. All rights reserved.
http://dx.doi.org/10.1016/j.physrep.2013.03.001

1. Introduction

Rogue waves are extreme events occurring in systems characterized by the presence of many waves. They are rare events, the most known examples being the extreme events that seldom, and unpredictably, appear on the ocean surfaces. The terms "rogue" or "freak" waves have, indeed, been coined in this context, where these extreme events constitute a well-known, and frightening, phenomenon, leading to water walls as tall as 20–30 m and representing a threat even for large boats and ocean liners [1,2]. The origin of rogue waves is still a matter of debate [3] and a large interest has grown in the last years that has brought to the development of different theoretical approaches as well as to setup different kind of laboratory experiments.

Several models have been developed, most of them relying on the weak nonlinear interaction between many waves and, thus, based on the nonlinear Schrödinger equation [4,5]. However, such envelope equation approaches may fail to catch the very steep profile that characterizes the extreme events. In this context, numerical simulations play an important role shedding light on basically involved mechanisms, as the role of large breathers [6] and the emergence of extreme events from wave turbulence [7]. Recently, large scale experiments have been performed to study directional ocean waves [8], and the steadily growing interest in the subject has led to study rogue waves in laboratory experiments and in many different

systems, as nonlinear light propagation in doped fibers [9,10], acoustic turbulence [11], nonlinear optical cavities [12] and microwave transport [13].

The common feature characterizing rogue wave phenomena in the different systems is the observation of large deviations from the Gaussian statistics of the wave amplitude, with long tails of the probability density function (PDF) accounting for the rather frequent emission of the giant waves. Despite the specificity of each experiment, other common properties can be identified, as the existence of many uncorrelated "grains" of activity that are inhomogeneously distributed in larger spatial domains. Depending on the system under study and on the nature of the waves considered, grains can be of a different origin, for instance, solitons in nonlinear systems or wave packets in linear propagating waves, and their clustering in spatial domains can occur via different mechanisms, as a temporal delay, a spatial symmetry breaking, a transport phenomenon or a hypercycle type amplification [14].

On the other hand, it has been recently outlined in the microwave experiment that rogue waves can occur even in the absence of nonlinearity [13]. It seems, therefore, that nonlinearity has the role of bringing forth granularity, that is, of inducing soliton-like structures. In order to verify this conjecture, a linear optical experiment has been developed and the outcomes have been compared to those from a nonlinear cavity [15]. The results show that the appearance of rogue waves is related to the presence, in the system, of a suitable amount of granularity and inhomogeneity, independently if they are induced by a linear or a nonlinear mechanism.

2. Introduction to the statistical properties of ocean waves

The dynamics of ocean waves is described by a set of partial differential equations, known as the Navier–Stokes equations, that account for the conservation of mass and momentum applied to a fluid considered as a continuum. The solution of such system is challenging and, even under the hypotheses that the atmosphere is decoupled from the ocean, the equations are not easily tractable from an analytical and numerical point of view. This is mostly related to the fact that one must impose the boundary conditions on the free surface in order to describe the evolution in time and space of the perturbations that takes place on the surface itself. The boundary conditions requires that the surface is impermeable (water particle cannot leave the surface) and, in the inviscid limit, the pressure is a continuous function across it. Mathematically speaking, the boundary conditions results in two evolution equations, one for the surface elevation and one for the velocity potential calculated on the surface. The peculiarity of these equations is that they are both nonlinear. Only under the hypothesis of small amplitude waves (with respect to the wavelength) the equations can be linearized and the linear dispersion relation can be worked out in a straightforward manner. If h is the water depth, then the angular frequency, ω, and the wave number k are related as follows:

$$\omega = \sqrt{gk \tanh(kh)}, \tag{1}$$

with g the gravity acceleration. It is customs in the ocean wave community to treat separately the deep and the shallow water regimes; if $kh \to \infty$ waves are considered in deep water and $\omega \simeq \sqrt{gk}$; if $kh \to 0$ waves are in shallow water waves and the dispersion relation takes the form $\omega \simeq \sqrt{gh}k\left(1 - \frac{h^2k^2}{6}\right)$. As it will be clear later, such distinction will become useful in the description of the mechanisms of formation the rogue wave formation: while in deep water self-focusing phenomena (local concentration of energy due to nonlinear interactions) can take place naturally, shallow water are stable and, as it will be shown, the nonlinearity is of de-focusing type. Except for the very shallow water regime, ocean waves are dispersive: long waves travel faster than short waves. Such mechanism has been used for decades for producing rogue waves in wave tank facilities: the idea is to generate first short waves that are then caught up by longer waves. If the experiment is well designed, at some distance from the wave maker, all waves generated are in phase and can be summed-up (linear superposition principle) to generate a large amplitude wave (see for example [16–18]).

The idea has also been extended to two horizontal dimensions both in laboratory [19] and in numerical computations [20]. Note that the nonlinearity cannot be neglected completely because during the late stages of the formation of the extreme wave the steepness is not a small parameter anymore and the small amplitude approximation fails. The generation of waves through such linear mechanism is very useful in laboratory tests; however, from an oceanographic point of view it appears artificial because it needs an *ad hoc* preparation of the phases for each Fourier component. Oceanographers have historically treated the surface waves as a homogeneous and stationary stochastic processes characterized by Fourier phases uniformly distributed in the $[0, 2\pi)$ interval, [21,22]. In the linear approximation, the wave components are assumed to be independent from each other and, according to the central limit theorem, the surface elevation is characterized by a probability density function which is approximately Gaussian. On a statistical bases, the phases in principle can assume the same value, but the probability of such event is rare and it will be discussed in more details in Section 2.2. Should the waves show some correlation at an hypothetical initial time, such correlation would decrease exponentially fast due to linear dispersion [22]. Linear superposition has attracted the attention of many oceanographers working on rogue waves; in the present review we will not consider it furthermore and we redirect the reader to the excellent book by C. Kharif et al. [23].

2.1. The wave spectrum

Before entering into the discussion on the effects of nonlinearity, we introduce some oceanographic terminology that it is often encountered in rogue waves papers; hereafter a short digression on the ocean wave spectrum and related quantities is

furnished. The shape of the interface between water and air is described by the function $\eta(\mathbf{x}, t)$ where the vector $\mathbf{x} = (x, y)$ corresponds to the horizontal coordinates and t is time. Given the simultaneous observation of the surface displacement $\eta(\mathbf{x})$ at two different spatial points, $\mathbf{x_1}, \mathbf{x_2}$, such that $\mathbf{r} = \mathbf{x_1} - \mathbf{x_2}$, one can introduce the two-point correlation function, $\langle \eta(\mathbf{x_1})\eta(\mathbf{x_2})\rangle$, where the brackets implies ensemble averaging. Assuming homogeneity of the wave field, the two-point correlation function depends only on the distance $\mathbf{r}$ and can be defined as:

$$R(\mathbf{r}) = \langle \eta(\mathbf{x} + \mathbf{r})\eta(\mathbf{x})\rangle. \tag{2}$$

The two dimensional wave number spectrum, $P(\mathbf{k})$, is related to the autocorrelation function via the Fourier Transform:

$$R(\mathbf{r}) = \int P(\mathbf{k}) \exp(i\mathbf{k} \cdot \mathbf{r}) d\mathbf{k} \tag{3}$$

such that

$$\rho g \langle \eta^2 \rangle = \rho g R(0) = \rho g \int P(\mathbf{k}) d\mathbf{k}, \tag{4}$$

with ρ the fluid density. The quantity on the left is the total (kinetic + potential) energy in the wave field, therefore the wavenumber spectrum furnishes the distribution of energy over wavenumbers. Even though an estimate from experiments of $P(\mathbf{k})$ is possible [24], it is much more common and simple in the oceanographic research to place a wave recorder (for example a buoy) in a fixed position and measure the surface displacement as a function of time. If the time series is sufficiently long and stationary, such measurement leads to a straight forward estimate of the frequency spectrum. More in general, the two dimensional frequency spectrum is related to the two dimensional wave number spectrum as follows:

$$P(\mathbf{k})d\mathbf{k} = P(k, \theta)dkd\theta = P(\omega, \theta)d\omega d\theta, \tag{5}$$

where k and θ are the two polar coordinates. From a single point measurement it is impossible to retrieve the directional information of the wave fields and only the frequency spectrum, $P(\omega)$, defined as:

$$P(\omega) = \int_0^{2\pi} P(\omega, \theta) d\theta, \tag{6}$$

is available. During the sixties and seventies the parametrization of the shape of $P(\omega)$ and its dependence on wind and fetch (distance over which wind has blown) has been a major experimental task. The most important experiment was conducted in the North Sea by the JONSWAP (Joint North Sea Wave Project) group [25]. The empirical distribution proposed is the following:

$$P_{JON}(\omega) = \frac{\alpha g^2}{\omega^5} \exp\left[-\frac{5}{4}\left(\frac{\omega_p}{\omega}\right)^4\right] \gamma^{\exp\left[-\frac{(\omega-\omega_p)^2}{2\sigma^2\omega_p^2}\right]} \tag{7}$$

where $\sigma = 0.07$ if $\omega \leq \omega_p$ and $\sigma = 0.09$ if $\omega > \omega_p$. The α, γ and σ were originally obtained by fitting the experimental data. Here ω_p is the angular frequency corresponding to the peak of the spectrum, γ is the so called "enhancement" factor and α is the Phillips parameter which is related to the energy of the wave field. In Fig. 1 we show the JONSWAP spectrum for different values of $\gamma = 1, 3, 6$, $\omega_p = \pi/6$ rad/s and $\alpha = 0.0081$. From the figure is clear that, as γ increases, the spectrum becomes more energetic and narrower around the spectral peak. As will become clear in the next sections, this will have some consequences on the formation of rogue waves in the ocean.

The determination of the angular distribution of the frequency wave spectrum is not an easy task. Arrays of wave gauges or directional buoys are needed and a post processing procedure has to be employed in order to extract the energy angular dependence. Without entering into the details of the difficulties of such estimate [26], the directional frequency spectrum is usually parametrized by factorizing its angular dependence. For the purpose of the present review it is sufficient to report the following simple form of the directional frequency spectrum:

$$P(\omega, \theta) = P_{JON}(\omega) B(N) \cos^N(\theta), \tag{8}$$

which has been recently used in experimental studies of rogue waves [27,8]. $B(N)$ is a normalization coefficient such that the integral over angle is 1. In Fig. 2 we show the angular distribution of wave energy. For large values of N wave almost unidirectional and are known as long crested. For small N, the distribution of energy in angle is wide and the waves are known as short crested.

2.2. Rayleigh distribution for the wave envelope: linear theory

As discussed in the previous section, the wave field at fixed location is described by the superposition of a large number of wave components with different frequencies. If the waves are characterized by a small amplitude, then components are

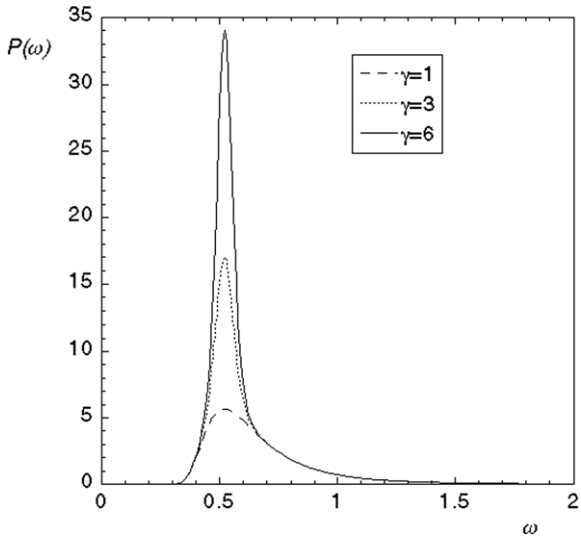

Fig. 1. The JONSWAP spectrum for different values of γ.

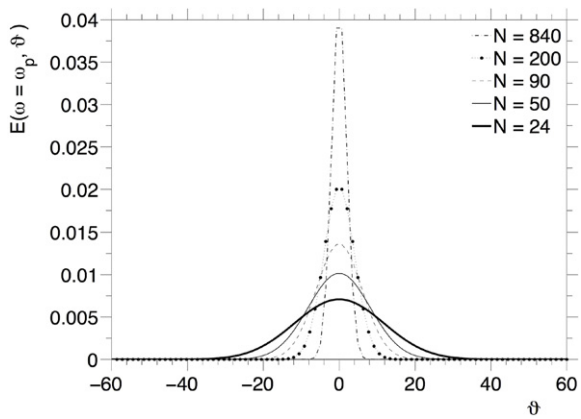

Fig. 2. Wave energy density angular distribution for different values of N.

de-correlated and the resulting surface elevation, $\eta(t)$, is described by a Gaussian distribution. Under such hypothesis, one can calculate the distribution for the wave envelope $A(t)$ which is related to the surface elevation as follows:

$$\eta(t) = A(t)\cos[\theta(t)]. \tag{9}$$

One way of approaching the problem consists in introducing the auxiliary variable, $\zeta(t)$,

$$\zeta(t) = A(t)\sin[\theta(t)] \tag{10}$$

so that:

$$A(t) = \sqrt{\eta(t)^2 + \zeta(t)^2}, \qquad \theta(t) = \arctan(\zeta(t)/\eta(t)). \tag{11}$$

By construction $\eta(t)$ and $\zeta(t)$ are de-correlated functions, both characterized by a Gaussian distribution, therefore their joint probability density function is:

$$p(\eta, \zeta) = \frac{1}{2\pi\sigma^2}\exp\left[-\frac{\eta^2 + \zeta^2}{2\sigma^2}\right] \tag{12}$$

with σ the standard deviation of η and ζ (both η and ζ are zero mean functions). From such probability one can compute the joint probability of the envelope and phases, $p(A, \theta) = Ap(\eta, \zeta)$ (the factor A comes from the Jacobian of the transformation to polar coordinates). The probability density function for the wave envelope is obtained by integrating over angles:

$$p(A) = \int_0^{2\pi} \frac{A}{2\pi\sigma^2}\exp\left[-\frac{A^2}{2\sigma^2}\right]d\theta = \frac{A}{\sigma^2}\exp\left[-\frac{A^2}{2\sigma^2}\right]. \tag{13}$$

The obtained distribution is called the Rayleigh distribution.

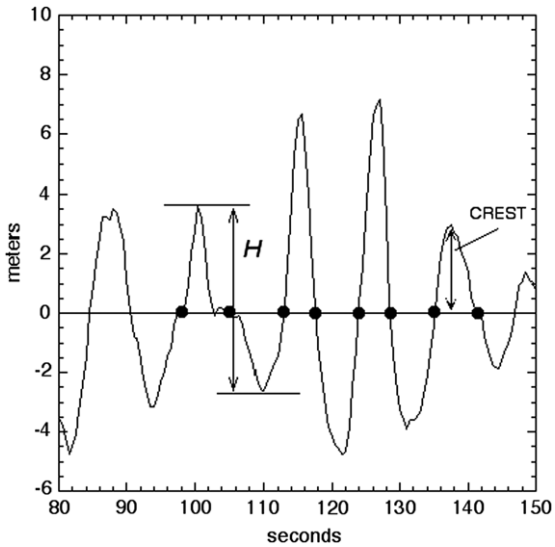

Fig. 3. An example of time series recorded in the ocean. The black dots indicate the zero crossing.

The envelope is a mathematical well defined quantity; however, oceanographers do not deal often with it and prefer to compute the statistics of wave heights, H. In order to illustrate this concept, we consider a time series as in Fig. 3, and look for the zero-crossing (the points in which the surface elevation is zero). The difference between the maximum value of the surface elevation in between two zero-crossing and the minimum value of the surface elevation in the adjacent (next or previous) zero crossing interval is called wave height. Clearly, for a linear narrow band process, $H \simeq 2A$, then the statistics of the envelope is closely related to the statistics of wave height. An other concept used by oceanographer is the significant wave height, H_s, introduced by W. Munk in 1944, [28] which expresses the wave height estimated by a "trained observer". Nowadays, it is a common rule to identify the significant wave height with 4σ; therefore, we will take it as a definition: $H_s = 4\sigma$.

In the oceanographic rogue wave context, often one is interested in addressing the problem on what is the probability of measuring (or encountering) a wave whose height is larger than some specific height H_0, i.e the exceedence probability or cumulative probability function defined as:

$$P(H > H_0) = \int_{H_0}^{\infty} \frac{H}{4\sigma^2} \exp\left[-\frac{H^2}{8\sigma^2}\right] dH = \exp\left[-\frac{H_0^2}{8\sigma^2}\right] = \exp\left[-2\frac{H_0^2}{H_s^2}\right]. \tag{14}$$

Sometimes in the literature, a rogue wave is defined as a wave such that $H > 2H_s$ (this definition is clearly not completely satisfactory and accepted in the oceanographic and naval architecture community because it would for example identify a 20 cm wave as a rogue wave if the significant wave height is 10 cm!!). According to Eq. (14), then its probability turns out to be 1/2980. For ocean waves characterized by a dominant period of 10 s, this implies that in approximately 8.2 h one expect to encounter one of such waves. As will be shown later, nonlinear interactions will modify such probability. An other quantity that oceanographers and naval architectures are interested in are the wave crests and wave troughs; given two successive zero crossing, the maximum/minimum between those two points is the wave crest/trough. In linear theory the statistics of the troughs is identical to the crests and both are described by a Rayleigh distribution. Second order nonlinearity changes the statistics of crests (and troughs); in the narrow band approximation the so called Tayfun distribution [29] can be derived starting from the second order Stokes expansion. The resulting distribution accounts for the vertical asymmetry that characterizes ocean waves.

3. Experimental evidence of rogue waves in the ocean

While there are a lot of visual observation of rogue waves [30], field measurements are less common. The most impressive and studied one is probably the "Draupner wave" (see for example [31]). On January 1 1995, the Statoil Draupner platform was hit by a giant wave. The water depth in the area is about 70 m. The wave was measured by a down-looking laser device and the significant wave height averaged over 20 min was about 11.9 m. The maximum wave height was 26 m, but probably the most impressive result is that its crest was 18.5 m (Fig. 4). In [32] seven cases of rogue waves, including the Draupner wave, are reported (time series are shown in the paper). Those waves, recorded in the North Sea (see also [33] for further analysis), in finite depth conditions, all show very large crests with respect to the significant wave height of the time series (such ratio ranges from 1.24 to 1.75). Rogue waves have also been measured off the coast of Brazil, in Campos Basin. A discussion of the data is found in [34]. From the 7457 available data sets each of approximately 17 min, they obtained 276

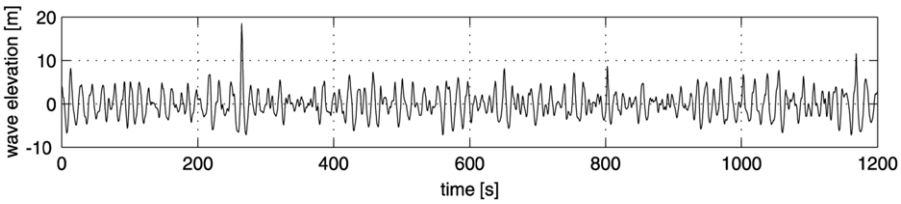

Fig. 4. The Draupner time series.

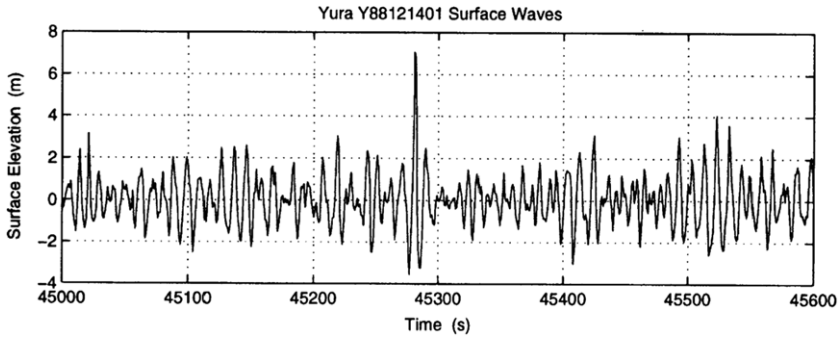

Fig. 5. Yura wave.
Source: From [35].

distinctive cases of waves larger than 2 times H_s. The measurements are performed with a directional buoy, therefore, in principle, directional information are available.

Three kilometers off the Yura fishing harbor facing the Sea of Japan, analysis of field data have also reveal the presence of rogue waves, [35,36]; an example is given in Fig. 5. In [35] it was found that the crest and trough amplitude distributions of the observed sea waves, including the freak ones, are different from the Rayleigh distribution, although the wave height distribution tends to agree with the Rayleigh distribution.

As a general comments, we may state that waves whose height is larger than two times (and more) the significant wave height have been recorded in field measurements (this is not a surprise even in a linear system). The experimental data, as they are, do not furnish any information on the physical mechanism of formation of such waves. Moreover, more than often, the time records last 20 min, surely not enough for achieving the convergence of the statistics on the tails of the probability density function and for observing possibly the deviation from the Rayleigh distribution. A physical understanding of the formation of the rogue wave would require space–time measurements. In 2004 in [37,38] it has been proposed a method to derive two-dimensional sea surface elevation fields from complex synthetic aperture radar (SAR) data. According to [37], once applied to spaceborne SAR data, as those acquired by European Remote Sensing 2 (ERS-2) or the Environmental Satellite (ENVISAT), the method allows to analyze the structure of ocean wave fields, e.g., wave grouping or individual wave heights on a global scale and possibly rogue waves. However, in [39] it has been argued that this is not possible. The main reason is that the SAR imaging mechanism is, in general, strongly nonlinear; thus the SAR image of the ocean wave field is a distorted image of the ocean wave field which bears little resemblance with the actual ocean wave field [39]. Wave radars [40] located on platform or ships offer an alternative for measuring the surface elevation and potentially rogue waves; however, more research is need in order to establish the accuracy of such type of measurements.

4. Nonlinearity and rogue waves in one horizontal dimension

The intrinsic nonlinearity of the ocean wave dynamics plays an important role in assessing the departure from Gaussian statistics of the surface elevation. Two types of nonlinearities can possibly be associated to the surface elevation: the first one is the result of the presence of the so called bound (or phase locked) modes. Those modes, as will become clearer in the next section, are the ones responsible of a vertical asymmetry of the surface elevation; anyone who has observed carefully ocean waves has realized that wave crests are sharper and narrower than wave troughs: this is especially true for waves in the shallow water regime. Such distorted shape is the result of a superposition of a primary sinusoidal wave with an infinite number of harmonics (the Stokes expansion). The harmonics have an amplitude that is a function of the primary wave and have the same initial phase. They do not obey to the linear dispersion relation. In terms of the statistical properties of the surface elevation, the role of the bound modes is to produce a positive skewness in the probability density function of the surface elevation. Bound modes do not interact in a dynamical sense and are phase lock to free modes (primary waves) whose interaction is the second source of departure from Gaussian statistics of the surface elevation. Indeed, it has been shown in [41] that quasi-resonant interaction between free modes may result in an increase (in deep water) or a decrease

(in shallow water) of the kurtosis with respect to its Gaussian value. The underneath mechanism of increasing the kurtosis in the random wave context is a generalization of the modulational instability processes. In the following sections these aspects will be considered in details in the framework of the Nonlinear Schrödinger equation, NLS.

4.1. The nonlinear Schrödinger equation for water waves in infinite water depth

Under the hypothesis of irrotational flow and inviscid fluid, the dynamics of a free surface flow is described by the Laplace equation for the velocity potential, by two boundary conditions (dynamic and kinematic) on the free surface and by one on the bottom. Even though the Laplace equation is linear, the boundary conditions on the free surface are not: this makes the problem much more difficult to solve and, at the same time, much more attractive and rich in terms of physical phenomena. Only under the assumption of very small amplitude waves (steepness) the problem can be linearized. Ocean waves, forced by winds, are usually characterized by an average steepness $\epsilon = H_s k_p/2$ of about 0.1, with k_p the wavenumber corresponding to the peak frequency of the spectrum; single waves hardly survive to steepnesses larger than 0.4 [42]. Even though the wave breaking is a strongly nonlinear process, its final effect is to keep the water wave dynamics in a statistically weakly nonlinear regime (this justify the weakly nonlinear approach).

The standard way of deriving the NLS equation from primitive equations of motion is to expand the surface elevation and the velocity potential in power series and use the multiple scale method; the idea is to introduce slow independent variables (both for time and space) and treat each of them as independent. The extra degrees of freedom arising from such variables allows one to remove the secular terms that may appear in the standard expansion. The multiple scale expansion is usually performed in physical space and a simplification of the procedure is the requirement that the waves are quasi-monochromatic. Indeed, in infinite water depth, if such procedure is performed it turns out that the surface elevation up to third order in nonlinearity takes the following form (see for example [43]):

$$\eta(x,t) = \left(|A(x,t)| - \frac{1}{8}k_0^2|A(x,t)|^3\right)\cos(\theta) + \frac{1}{2}k_0|A(x,t)|^2\cos(2\theta) + \frac{3}{8}k_0^2|A(x,t)|^3\cos(3\theta) + \cdots \tag{15}$$

$A(x,t)$ is the complex wave envelope, k_0 is the wave number of the carrier wave and $\theta = k_0x - \Omega_0 t + \phi$, ϕ is a phase, $\Omega_0 = \omega_0(1 + k_0^2|A(x,t)|^2/2)$ is the nonlinear dispersion relation, with $\omega_0 = \sqrt{gk_0}$ and g the gravity acceleration. The amplitude and the phase of the higher harmonics are fixed once the amplitude and the phase of the primary wave are established; the higher order modes are called bound modes (or slave modes), while the primary one is a free mode. Note the presence of a correction to the first harmonic arising from the third order nonlinearity. If $A(x,t)$ is constant, then (15) is known as the third order Stokes wave. The complex envelope obeys to the NLS equation:

$$i\left(\frac{\partial A}{\partial t} + c_g\frac{\partial A}{\partial x}\right) - \frac{\omega_0}{8k_0^2}\frac{\partial^2 A}{\partial x^2} - \frac{1}{2}\omega_0 k_0^2|A|^2 A = 0. \tag{16}$$

$c_g = \partial\omega/\partial k$ is the group velocity. The second term takes into account the dispersive behavior of the surface elevation, while the last one is the nonlinear term. The NLS equation is an integrable equation via the Inverse Scattering Transform and such property has been used also in the rogue wave context to identify rogue waves in random wave trains [44–47].

If one is interested in comparing the NLS simulations with experimental results in wave tank facilities, it is a common practice to write the NLS equation as an evolution equation in space rather than in time. In order to derive such equation one uses the leading order relation

$$\frac{\partial A}{\partial x} \simeq -\frac{1}{c_g}\frac{\partial A}{\partial t} \tag{17}$$

to calculate the second order derivative in the dispersive term. The evolution equation in space has the following form:

$$i\left(\frac{\partial A}{\partial x} + \frac{1}{c_g}\frac{\partial A}{\partial t}\right) - \frac{k_0}{\omega_0^2}\frac{\partial^2 A}{\partial t^2} - k_0^3|A|^2 A = 0. \tag{18}$$

The resulting equation is similar to the one that is usually presented in nonlinear optics.

4.1.1. The NLS in nondimensional form: the Benjamin–Feir-Index

In classical fluid mechanics it is a common practice to introduce nondimensional numbers that immediately furnishes some information on the flow conditions. The standard way of obtaining such numbers is to write the equations in nondimensional form by introducing characteristics scales of the relevant physical quantities of the problem. For example, the Reynolds number is obtained by scaling in an appropriate way the Navier–Stokes equation. We approach the Eq. (16) in a similar way and scale the variable x with a typical length, L, which is of the order of the wave packet length, and the amplitude of the wave with a characteristics wave amplitude, a_0, so that to obtain the following nondimensional variables identified by primes:

$$x' = \frac{x}{L}, \qquad A' = \frac{A}{a_0}, \qquad t' = \frac{\omega_0}{8k_0^2L^2}t \tag{19}$$

(the reason why time is scaled in that way becomes obvious when the previous scalings are introduced in Eq. (16)). The NLS equation, for nondimensional variables, in a coordinate system moving with the group velocity, takes the following form:

$$i\frac{\partial A}{\partial t} - \frac{\partial^2 A}{\partial x^2} - (2k_0a_0)^2(k_0L)^2|A|^2A = 0, \tag{20}$$

where the primes have been omitted for simplicity. Note that in this form the nonlinear term in NLS equation is multiplied by a nondimensional number which includes the product of the steepness by the nondimensional length of the wave group. We expect the nonlinearity to be important if such product is large.

Ocean waves are composed by different wave packets whose lengths are variable but in average are related to the spectral bandwidth: therefore, if we introduce Δk as a typical spectral bandwidth, then $L \sim \Delta k^{-1}$. Having this in mind and using the nondimensional number in Eq. (20), one may introduce the so called Benjamin–Feir-Index as:

$$\mathrm{BFI} = 2\sqrt{2}\frac{k_0a_0}{\Delta k/k_0} = \sqrt{2}\frac{k_0a_0}{\Delta\omega/\omega_0}, \tag{21}$$

which is nothing than the square root of the nondimensional number that appears in (20) (a factor of $\sqrt{2}$ has been included in order to match an exact analytical result which will be presented later). The last equality results from the fact that in deep water the group velocity is half of the phase velocity. k_0a_0 is now the average steepness of the random waves that can be estimated as $k_0a_0 = H_sk_p/2$ where k_p is the wave number corresponding to the spectral peak and H_s the significant wave height. The above derivation has been proposed originally in [4], where it has been shown numerically that for initial conditions characterized by large BFI, the probability of finding extreme waves increases. A more formal way of relating freak waves to the BFI has been introduced a couple of years later [41] and will be discussed in the Section 4.6.

4.2. The modulational instability

The modulational instability, also known as the Benjamin–Feir instability, has been discovered in the water wave context in the late sixties independently by Benjamin and Feir [48] and Zakharov [49]; see [50] for an historical review on the subject and possible applications. It describes the exponential growth of an initially sinusoidal long wave perturbation of a plane wave (Stokes wave) solution of the one dimensional water wave problem. The condition of instability in infinite water depth is that $2\sqrt{2}A_0k_0N > 1$, where A_0 is the amplitude of the plane wave and k_0 is the corresponding wave number; $N = k_0/K$ is the number of waves under the perturbation of wavenumber K. The modulational instability is frequently studied within the nonlinear Schrödinger equation that describes weakly nonlinear and dispersive waves in the narrow band approximation. In this context, the nonlinear stage of the modulational instability is described by an exact solution of the NLS, known as breather [51,52]. Such waves have been considered as prototypes of rogue waves [53,54]. More recently the modulational instability has been also considered as a wave breaking mechanism [55]. Indeed, if the initial steepness of the monochromatic wave is large, during the process of modulational instability, one wave will start growing and will soon reach the limiting steepness, and break much before becoming a rogue wave.

4.3. Breather solutions

(i) *The Peregrine solution*

The Peregrine solution, also known as rational solution, has been originally proposed in [56]. It has the peculiarity of being not periodic in time and in space: it is a wave that "appears from nowhere and disappears without trace" [57]; its maximum amplitude reaches three times the amplitude of the unperturbed waves. For the above reasons it has been considered as special prototype of freak wave, [58]. The Peregrine solution has been recently reproduced experimentally in wave tank laboratories [59] and in optical fibers [60]. Recent experiments have also reported the evidence of Peregrine solitons in plasmas [61].

Below we present its analytical form:

$$A(x,t) = A_0\exp\left[-i\beta A_0^2t\right]\left(\frac{4\alpha(1-i2\beta A_0^2t)}{\alpha+\alpha(2\beta A_0^2t)^2+2\beta A_0^2(x-c_gt)^2} - 1\right) \tag{22}$$

here α and β are the coefficient of the dispersive and nonlinear term in (16), respectively, i.e. in infinite water depth $\alpha = \omega_0/(8k_0^2)$ and $\beta = k_0\omega_0^2/2$. In Fig. 6 we show an example of such solution for steepness 0.1. Time is nondimensionalized by the wave period, space with wavelength and the amplitude with the A_0. Note that only the wave envelope is shown in the figure. The Peregrine solution is fully determined once the amplitude and the wavelength (i.e. the steepness) are selected. Independently of such choices, the amplification factor is always equal to three; the shape of the largest wave group changes depending on the initial steepness. The NLS theory does not predict the breaking or overturning of the waves: in principle a Peregrine solution of the NLS can be built with arbitrary steepness. In nature, steepness hardly reaches values larger than 0.4, [42], because of wave breaking; therefore, if one desires to generate a Peregrine solution in a wave tank, the initial condition should be characterized by a small steepness such that when the rogue wave appear, wave breaking does not

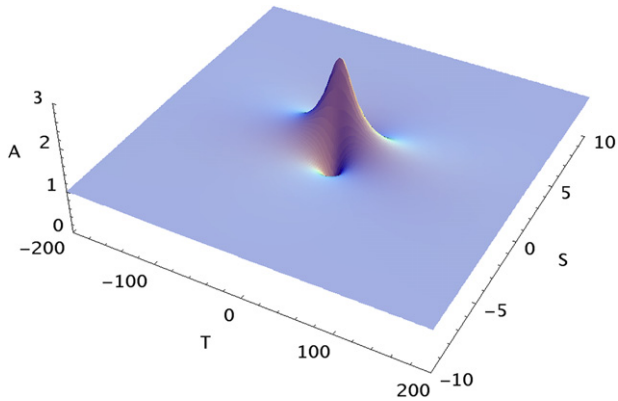

Fig. 6. The Peregrine soliton: normalized wave envelope as a function of nondimensional time and space.

occur. In spectral space the Peregrine solution is characterized, even at its early stages, by a triangular shape (see [62] for and experimental evidence). In [63,64] it has been proposed that such spectral shape could be used as an early warning of the presence of a rogue wave.

(ii) *The Akhmediev solution*

The Akhmediev breather is an exact solution of the NLS equation [65,66,51]; it describes the modulational instability in its nonlinear regime; it is periodic in space. It is characterized by an amplification factor which ranges from 1 to 3 (this last value corresponds to the Peregrine solution). The breather has the following analytical form:

$$A(x,t) = A_0 \exp\left[-i\beta A_0^2 t\right]\left(\frac{\sqrt{2}\tilde{\nu}^2\cosh[\Omega t] - i\sqrt{2}\tilde{\sigma}\sinh[\Omega t]}{\sqrt{2}\cosh[\Omega t] - \sqrt{2-\tilde{\nu}^2}\cos[Kx - c_g t]} - 1\right) \tag{23}$$

and

$$\tilde{\nu} = \frac{K}{A_0}\sqrt{\frac{\alpha}{\beta}}, \qquad \tilde{\sigma} = \tilde{\nu}\sqrt{2-\tilde{\nu}^2}, \qquad \Omega = \beta A_0^2\tilde{\sigma}, \tag{24}$$

K is the wave number of the perturbation. The solution is periodic in space. It is straightforward to show that for large negative times, the solution corresponds to $A_0\exp(i\phi)(1+\delta\cos(Kx))$, wit δ small; such solution corresponds to a perturbed Stokes wave. Ω corresponds to the exponential growth rate of the perturbation. The perturbation grows if $2-\tilde{\nu}^2 > 0$, which for deep water waves corresponds to the condition $K < 2\sqrt{2}A_0k_0^2$; not surprisingly such result corresponds to the standard one achieved by performing the linear stability analysis of a Stokes wave solution of the NLS equation. One can find the absolute maximum of the solution and after some algebra it is straightforward to show that

$$\frac{A_{max}}{A_0} = 1 + 2\sqrt{1-\frac{\tilde{\nu}^2}{2}} = 1 + 2\sqrt{1-\left(\frac{1}{2\sqrt{2}\epsilon k_0/K}\right)^2}. \tag{25}$$

The maximum amplitude reached when $\epsilon k_0/K = \epsilon N \to \infty$; for such case A_{max}/A_0 is equal to 3, i.e. the Peregrine solution. In the water wave context, the steepness ϵ is always less than one, therefore, in order to reach the limit one has to make a very long perturbation that includes a large number of waves under it. In Fig. 7 we show an example of such solution for steepness 0.1 and $k_0/K = 5$ with $A_{max}/A_0 = 2.4142\ldots$.

(iii) *The Kuznetsov–Ma solution*

The Kuznetsov–Ma solution [52,67] is periodic in time and decrease exponentially in space. In some previous literature, the same solution has been attributed only to Ma; Nevertheless Kuznetsov found it two years earlier. While for the Akhmediev breather the large time (positive or negative) limit is a plane wave plus a small perturbation, the modulation for the Kuznetsov–Ma breather is never small; therefore it does not corresponds to the classical Benjamin–Feir instability. The solution has the following analytical form:

$$A(x,t) = A_0 \exp\left[-i\beta A_0^2 t\right]\left(\frac{-\sqrt{2}\tilde{\mu}^2\cos[\Omega t] + i\sqrt{2}\tilde{\rho}\sin[\Omega t]}{\sqrt{2}\cos[\Omega t] - \sqrt{2+\tilde{\mu}^2}\cosh[Kx - c_g t]} - 1\right) \tag{26}$$

with

$$\tilde{\mu} = \frac{K}{A_0}\sqrt{\frac{\alpha}{\beta}}, \qquad \tilde{\rho} = \tilde{\mu}\sqrt{2+\tilde{\mu}^2}, \qquad \Omega = \beta A_0^2\tilde{\rho}. \tag{27}$$

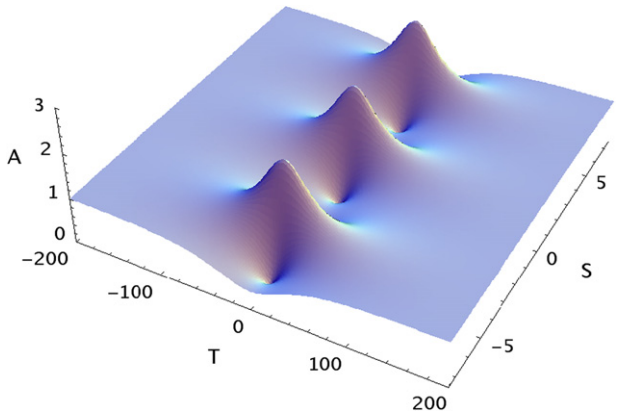

Fig. 7. The Akhmediev solution: normalized wave envelope as a function of nondimensional time and space.

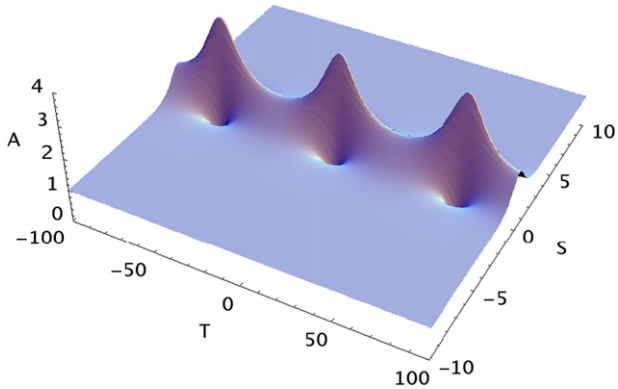

Fig. 8. The Kuznetsov–Ma solution: normalized wave envelope as a function of nondimensional time and space.

Just like for the Akhmediev breather one can find the maximum amplitude and obtain:

$$\frac{A_{max}}{A_0} = 1 + \sqrt{2}\sqrt{2 + \tilde{\mu}^2} = 1 + \sqrt{2}\sqrt{2 + \left(\frac{1}{2\epsilon k_0/K}\right)^2}. \tag{28}$$

In Fig. 8 we show an example of such solution for steepness 0.1and $\tilde{\mu} = \sqrt{2}$, which corresponds to a ratio $A_{max}A_0 = 3.8284$.

4.3.1. Relation between the breather solutions and standard solitons

As discussed for example in [53,68], the breather solutions are related. The Akhmediev solution becomes the Kuznetsov–Ma solution if K is replaced by iK. The Akhmediev and the Kuznetsov–Ma solution become the Peregrine solution in the limit of $K \to 0$. The Akhmediev solution becomes the plane wave solution if $\tilde{\nu} = \sqrt{2}$ and the Kuznetsov–Ma solution becomes a soliton in the limit of $K \to \infty$.

4.3.2. Higher order breathers

Nonlinear superposition of breather solutions is also possible. The NLS solutions associated with such mechanism are known as higher order solutions [65,69–72]. In [57] a method for finding the hierarchy of rational solutions of the self-focusing nonlinear Schrödinger equation is presented from first to fourth order. The maximum amplitude reached by the fourth order solution is 9. It appears that from a mathematical point of view there is no limitation in the amplification factor of the solution. In Fig. 9 a second order Peregrine solution is shown.

4.3.3. Experimental/numerical verification of the breather solutions in wave tanks

As just mentioned, an Akhmediev breather corresponds for large negative times to a sinusoidal wave for the surface elevation. Such breather solutions has been produced in laboratories, probably unconsciously, starting with the pioneering work by Yuen and Lake in the mid seventies, summarized in [74]. They did not realized that such solutions could be possibly related to the appearance of rogue waves in the ocean and their scope was mostly limited to the verification of the growth rates of the Benjamin–Feir instability within the nonlinear Schrödinger equation or higher order effects. Their work has

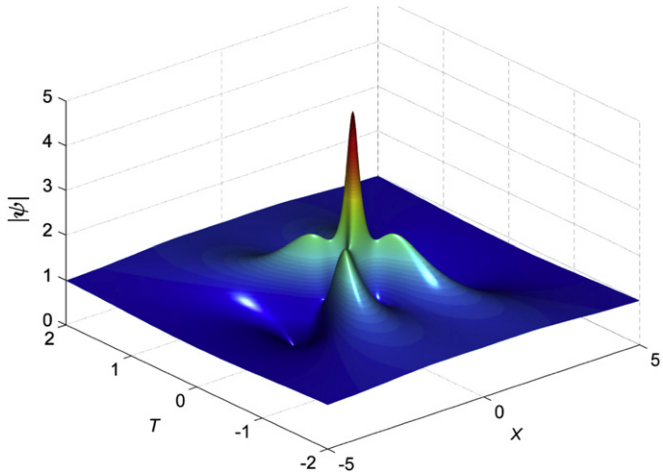

Fig. 9. Second order rational solution of the NLS The maximal amplification of five above the back-ground wave is 5.
Source: From [73].

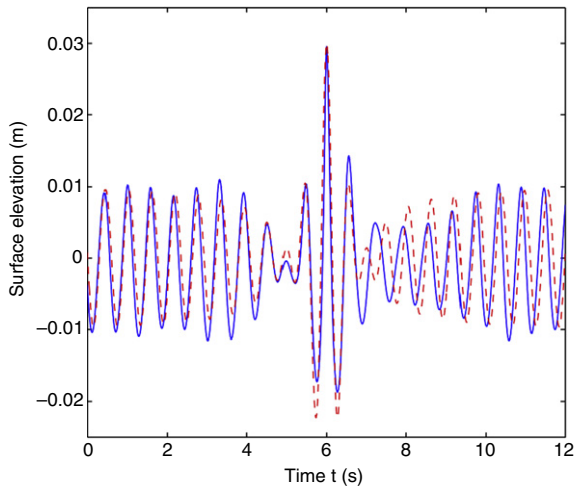

Fig. 10. Comparison of measured surface height at the position of maximum rogue wave amplitude (solid line) with the theoretical Peregrine solution (dashed line).
Source: From [59].

then been followed by a number of studies of which it is worth to quote the one performed by Tulin and Waseda [75] who systematically performed the so called "seeded experiments": instead of producing a monochromatic wave at the wave maker and let the most unstable mode develop along the tank, they have included small amplitude long perturbations, obtaining patterns corresponding, at least qualitatively, to the Akhmediev breathers. They also study the breaking of such solutions. It was only after the independent work in [53,54] that breather solutions have been brought up as rogue wave models. The Kuznetsov–Ma and the Akhmediev breathers were reproduced in March 2003, within the Large scale Facility Access project supported by the EU, in the MARINTEK (Trondheim) long wave tank facility [45]. A recent experimental study on the Akhmediev solution is also described [76]. As far as we know, the Peregrine solution with steepness 0.1 has been produced only recently in a short wave tank in the Hamburg University of Technology [59]. The experiments is performed in a water wave tank 15 m long and 1.6 m wide with 1 m water depth. The measurement and the exact solutions are shown in Fig. 10. The comparison seems more than satisfactory; the measured surface elevation, which naturally include second (and higher) order effects in terms of Stokes expansion, is compared directly with the leading order NLS solution without including the Stokes expansion (see (15)). The extraction of the free wave component from the measured time series would result in a slightly smaller maximum.

Recently, the Kuznetsov–Ma solution in intermediate water depth has been produced at the wave tank of the Technical University of Berlin [77] and used for sea keeping tests. As described later, it has been also observed in nonlinear optics experiment [78].

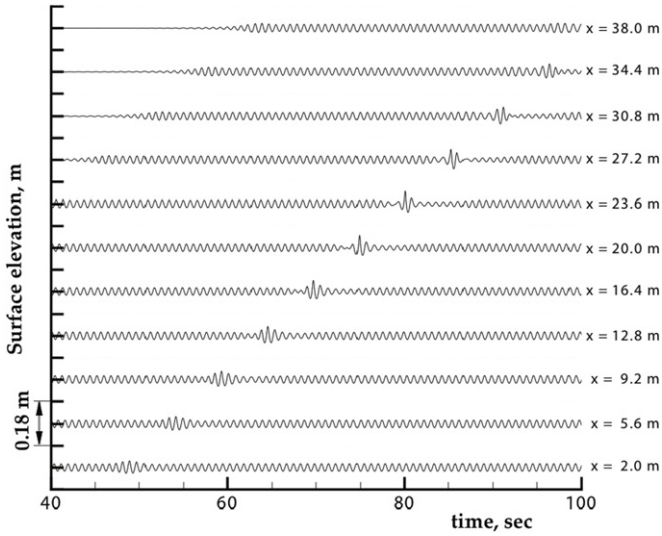

Fig. 11. Evolution of a Peregrine breather with steepness 0.1 and wave length 0.1 m.
Source: From [79].

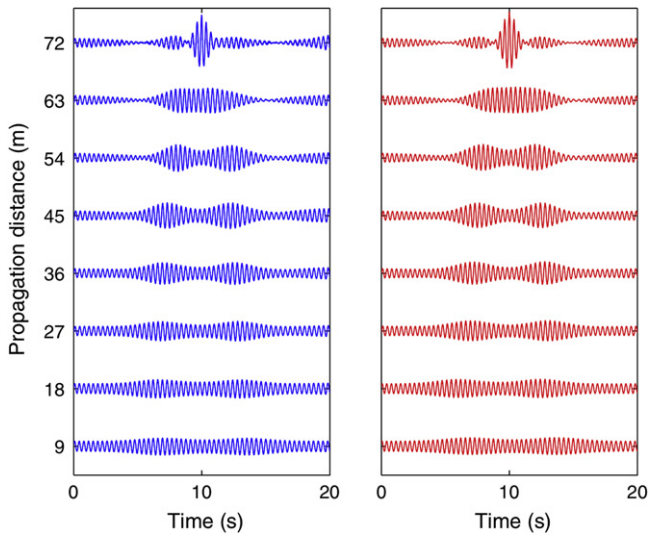

Fig. 12. Wave-profile evolution: the left panel shows experimental results while the right panel shows theoretical one.
Source: From [73].

Less expensive than wave tank experiments and very accurate are the results that can be obtained by the so called "numerical wave tanks", i.e. numerical simulations of the potential water wave problem which include the presence at one boundary of a wave maker. Such simulations have also the advantage that the surface elevation is available every where in the tank and not only in specific places were the wave gauges are placed. In this context the Peregrine solution have been simulated in 2006 [79]. Fig. 11 shows 11 time series recorded at different distances from the wave maker. Besides the formation of a large crest at $x = 20$ m from the wave maker, at 27.2 m a visible deep hole is displayed in the time series.

The second order Peregrine solution, known as super rogue wave, has been recently reproduced in a wave flume [73]. In Fig. 12 we show the experimental and exact solutions: as it is clear from the figure the super rogue wave appear as a nonlinear superposition of two breathers.

4.4. Finite depth effects

It is worth mentioning that the nonlinear Schrödinger equation presented in (16) is derived in the limit of infinite water depth, i.e. $k_0 h \to \infty$. An NLS equation in arbitrary depth has been derived in [80]. The group velocity and coefficients of the

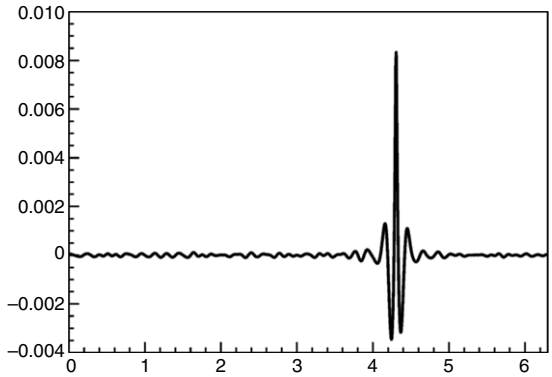

Fig. 13. Typical profile of a breather from the fully nonlinear potential equation. The initial condition is an NLS envelope soliton with large steepness. *Source:* From [6].

dispersive and nonlinear terms are also a function of water depth h and are reported below:

$$\begin{aligned} c_g &= \left.\frac{\partial\omega}{\partial k}\right|_{k_0} = \frac{ghk_0\,\mathrm{sech}^2[k_0h] + g\tanh[k_0h]}{2\omega_0} \\ \alpha &= \frac{1}{2\omega_0}\left(c_g^2 - gh\,\mathrm{sech}^2[k_0h](1 - k_0h\tanh(k_0h))\right) \\ \beta &= \frac{\omega_0k_0^2}{2}\left[\frac{(8+\cosh[4k_0h] - 2\tanh[k_0h]^2)}{8\sinh[k_0h]^4} - \frac{(2\omega_0\cosh[k_0h]^2 + k_0c_g)^2}{(k_0\sinh[2k_0h])^2(gh - c_g^2)}\right], \end{aligned} \tag{29}$$

with $\omega_0 = \sqrt{gk_0\tanh[k_0h]}$. The interesting thing is that the coefficient of the nonlinear term changes sign at $k_0h < 1.36$ from positive to negative and the NLS equation becomes of defocusing type and the waves are stable (no breather solutions exist but only dark solitons). The fact that unidirectional plane waves are stable for $k_0h < 1.36$ was recognized firstly in [48]. The consequences on rogue wave formation and prediction have been discussed in [81]. It should be mentioned that in two horizontal dimension, the modulational instability may persists also for depth smaller than 1.36 [82]. However, the transverse instability in shallow water has a very small growth rate and at the moment it is unknown if such instability can be associated to the formation of rogue waves.

4.5. The fully nonlinear approach in one horizontal dimension

A first comparison between the NLS simulations of unstable wave groups and fully nonlinear simulations is provided in [83]. The general idea is that the NLS equation describes accurately the surface elevation if the initial conditions are consistent with the hypotheses under which the equation has been derived, i.e. small steepness and narrow spectrum. However, as the steepness grows, differences between the exact solutions and the experimental or fully nonlinear results can be appreciated in particular in the symmetry properties of the wave envelope. It has been observed that an initial symmetric envelope evolves in an asymmetric one. This is not feasible within the NLS model, and it is well captured by including higher order nonlinear dispersive effects in the NLS equation (see [84]); the resulting equation is known as the Dysthe equation and has been widely used in the studies of rogue waves (in this review we will not treat specifically the Dysthe equation, see [85] for recent consideration on the equation). The long time evolution of long wave packets has been studied numerically in [86]. Fully nonlinear numerical simulations show how an initially long wave group slowly splits into a number of solitary wave groups. They occur during a time scale that is beyond the time range of validity of simplified equations like the NLS equation or modifications. Temporary downshiftings of the dominant wavenumber of the spectrum coincide with the formation of large wave events. The wave slope at maximal amplifications is about three times higher than the initial wave slope. The results show how rogue wave events can emerge from a long wave packet. A follow up of such idea has been considered also in [87,6]. The authors use a fast and accurate (probably the fastest and the most accurate existing) model based on conformal variables for solving the fully nonlinear potential equations for surface gravity waves. Numerical simulation demonstrates the existence of giant breathers on the surface of deep water.

The initial condition used in [6] is an NLS envelope soliton. However, the parameters of the soliton were chosen far beyond the applicability of the NLS equation. The simulation was performed in the periodic domain. As the initial NLS soliton propagates, the radiation is absorbed by an *ad hoc* damping. After some wave periods the damping is removed and the formation of single giant breather is observed, see Fig. 13. The numerical analysis shows that this breather does not loose energy in the fully nonlinear equations.

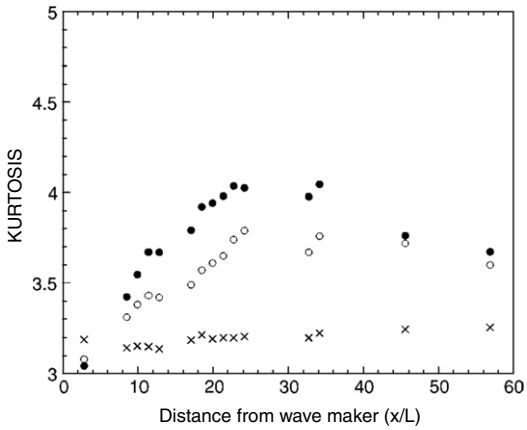

Fig. 14. Evolution of the kurtosis along the wave tank: BFI = 0.2, crosses; BFI = 0.9, empty circles; and BFI = 1.2, full circles. The horizontal axis has been nondimensionalized with the characteristic wavelength computed using the linear dispersion relation.
Source: From [89].

4.6. Rogue waves in random sea states

As mentioned in the introduction, real ocean waves are considered a stochastic process, therefore the concept of rogue wave just presented and based on the nonlinear stages of the Benjamin–Feir instability should be considered with care. A number of questions appear naturally: do breathers exists also in random wave trains? If yes, how do they naturally form? How much the randomness of the ocean destroys the coherency of such breathers? How does the presence of these breather alters the tails of the probability density function of wave height and wave crests? We will tray to answer these questions by showing some experimental works that has been performed in the last 10 years; moreover, some analytical predictions in the NLS framework on the skewness and the kurtosis which characterizes the tails of the surface elevation will also be presented. We will first concentrate on one dimensional propagation and then make some consideration on fully directional waves.

4.7. Some experimental results in wave tank laboratories for 1-dimensional propagation

The experimental work which will be briefly summarized has been performed in the long wave flume at Marintek, Trondheim (Norway). The length of the tank is 270 m and its width is 10.5 m. The depth of the tank is 10 m. A horizontally double-hinged flap type wave-maker located at one end of the tank was used to generate the waves. A sloping beach is located at the far end of the tank opposite the wave maker. The wave surface elevation was measured simultaneously by 19 probes placed at different locations along the flume. Twin-wire conductance measuring probes were used. The goal of the experiment was to highlight the concept of the Benjamin–Feir-Index (BFI) defined in (21) as the ratio of the steepness (nonlinear) and spectral bandwidth (dispersion) in the NLS equation, as a measure of the nonlinearity (of the modulational instability type) of the system. The idea is straightforward: a sea state characterized by a large BFI is more likely to contain rogue waves than a seas state with lower BFI. The experiments have been performed as follows: the wave maker is programmed in order to reproduced in front of it a surface elevation that is characterized by a JONSWAP spectrum (7) with random phases. The waves evolve along the wave tank and the surface elevation is measured at different distances from the wave maker. Statistical properties are then estimated from time series. Different repetition with a different set of random phases have been performed in order to increase the statistics. Three different JONSWAP spectra have been chosen characterized by different γ and α parameters in order to reproduced different seas states with different BFI. The results can be found in [88–90] (see also [91]). The BFI considered assumed the values 0.2, 0.9, 1.2. The evolution of the kurtosis along the tank is shown in Fig. 14. Waves are generated at the wave-maker with random phases and, because of the central limit theorem, for $x/\lambda = 0$, the amplitudes are Normal-distributed (the kurtosis is equal to 3). As the waves evolve along the tank there is a clear evidence that for the intermediate and large BFI the kurtosis increases and deviates substantially from the Normal value. Because the kurtosis is the fourth order moment of a probability density function, it carries some information on the tails of it; therefore, larger values of kurtosis indicates that rogue waves are more probable. As we will see in the next section an analytical formula relating the kurtosis and the BFI can be worked out within some approximations. A typical example of rogue wave measured in the wave tank is shown in Fig. 15. Those kind of events are much more frequent for BFI = 0.9 and BFI = 1.2 with respect to the case of BFI = 0.2. In Fig. 16, the probability of exceedence defined in (14) is shown. The plot shows a fattening of the tails of the probability of exceedence for larger values of BFI.

The results just presented leads to two main conclusions: (i) deviations from the expectation of the linear theory (Rayleigh distribution) are possible and systematically observed for long crested waves; (ii) stronger deviations are observed when the spectrum at the wave maker is characterized by larger BFI, i.e. large steepness and small spectral bandwidth. One may be

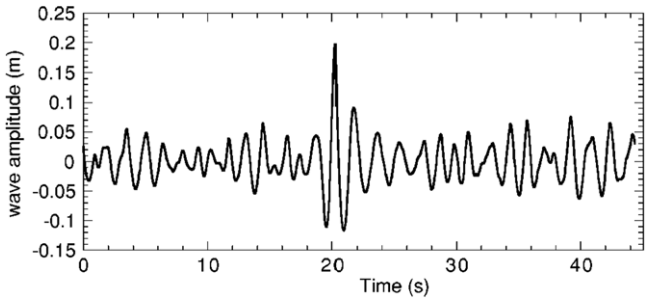

Fig. 15. Time series recorded for BFI = 1.2 at 32 wavelengths from the generator showing a rogue wave.
Source: From [88].

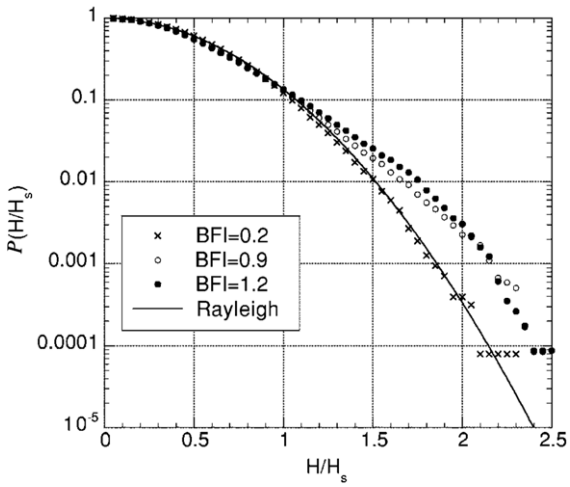

Fig. 16. Exceedence probability of wave height estimated from time series recorded at 32 wavelengths.
Source: From [88].

tempted to say that for each spectral shape one could associate a probability of occurrence of rogue waves: this consideration should be taken with some care because the spectrum evolves as the waves propagate along the tank: usually one observes a broadening of the spectrum during the evolution (see [92]), therefore the BFI is not constant and probably is not as large in the middle of the tank (where rogue waves are measured) as it is at the wave-maker. With more confidence one may state that the appearance of rogue waves depends on the history of the spectrum and not on the spectrum its self. A narrow and energetic initial spectrum (large BFI) with random phases will generate in more or less 30 wave lengths a highly non Gaussian statistics even though at such distance the BFI is not large anymore.

One of the important goal in both engineering and scientific research is the determination of the probability density function of wave height. In the view of what has been presented, it is obvious that any theoretical approach would have to deal with non small corrections to the Rayleigh distribution. In practice this important task has not been achieve yet. Many parametrization for the wave height distribution exists, each fitting the data for which they have been developed. Some systematic approach which include nonlinear corrections to the Rayleigh distribution have been started in [93], followed then in [94,95]. The idea is to include in the probability of wave height also a contribution from the fact that the kurtosis does not assume the Normal value. Results are encouraging when applied to experimental data [96], however a detail analysis performed in [97] indicates that the statistics of wave envelopes with theoretical expectation is "somewhat poor, particularly in the presence of relatively strong instabilities".

From the Marintek experimental data, also the statistics of wave crests have been analyzed in [90] and compared with second order theory, i.e. a description of the surface elevation based on the fact that the spectrum is frozen and only second order bound, components, see (15), contribute to deviation from Normal statistics. The results show that any second order theory strongly underestimate the tails of the crest distribution for large BFI.

The experimental results just described highlight the fact that in one dimensional wave systems strong deviations from linear predictions can be observed for large BFI. At the moment none of the existing theory is capable of describing accurately the tails of wave height and wave crest distributions. The origin of such deviation resides in the natural formation of unstable wave packets (similar to the breather solution of the NLS). In order to achieve a large BFI one has to decrease the spectral bandwidth, increasing the correlation lengths of the wave packets. Those coherent wave packets, if sufficiently energetic (large steepness), may become unstable and their envelope can be locally amplified; phase correlations during this process

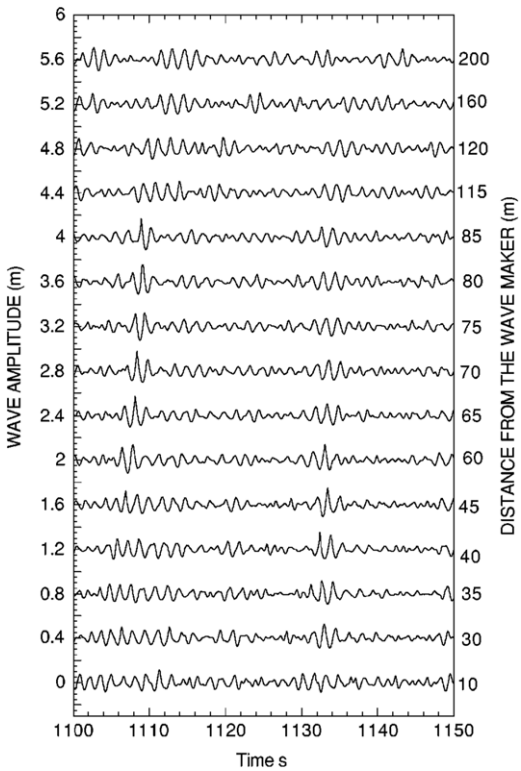

Fig. 17. Time series recorded at different probes. Time series, starting from the second probe, have been shifted by adding a constant amplitude in order to visualize them in the same graph. Time series have also been shifted in time in order to follow the evolution of the wave groups.
Source: From [89].

can be observed, [98]. An example of this phenomenology is shown in Fig. 17 where different time series recorded at various distances from the wave maker are displayed. A wave packet between 1100 and 1110 s became unstable, giving origin to a rogue wave. Note also at 75 m from the wave-maker the presence of a "hole in the sea".

In the next section we will show that, within some approximations, there is a formal relation between the BFI and the kurtosis.

5. Kurtosis and skewness of the surface elevation

5.1. The contribution to the kurtosis from free modes

Strong deviation from the Normal statistics in random one dimensional sea surface system is related to the cubic nonlinearity in the equation of motions. This was already observed through numerical computations [99,100] of the potential water wave problem using the so called Higher Order Spectral Method [101,102], i.e. a numerical method that allows one to include in a systematic way the desired order of accuracy in nonlinearity in the solution. However, a direct connection between the observed numerical or experimental deviations from Normal statistics and the third order nonlinearity has been pointed out in the seminole paper by P.A.E.M. Janssen [41] starting from the Hamiltonian formulation of surface gravity waves. The calculation requires a number of hypothesis: (i) The wave field must be homogeneous. (ii) Because of the nonlinearity of the problem, the calculation of the fourth order correlator automatically requires the knowledge of the sixth order correlator; therefore, a closure is needed to split the latter as a sum of the product of second order correlators (the spectrum). (iii) The large time limit is taken. Under such hypotheses, if one assumes that the wave spectrum is narrow and has the shape of a Gaussian function, frozen in time, the following elegant result for the kurtosis is obtained [41,95]:

$$\kappa^{(dyn)} = \frac{\langle \eta^4 \rangle}{\langle \eta^2 \rangle^2} = 3 + \frac{\pi}{\sqrt{3}} \left(\frac{\sqrt{2} k_0 \sqrt{\langle \eta^2 \rangle}}{\Delta\omega/\omega_0} \right)^2 = 3 + \frac{\pi}{\sqrt{3}} \mathrm{BFI}^2 \tag{30}$$

with $\Delta\omega$ the standard deviation of the Gaussian (i.e. related to the width of the spectrum) and ω_0 is the mean value of the Gaussian corresponding to the peak angular frequency. $k_0\sqrt{\langle \eta^2 \rangle}$ is a statistical measure of the steepness of the waves. Note that the superscript (dyn) on κ indicates that the kurtosis is the result of a dynamical process (basically a modulational

instability) and should not be confused from the kurtosis $\kappa^{(bound)}$ that is the result of bound (or slave) modes. For cubic nonlinearity the contribution to the skewness from the dynamics is zero.

The main point to be underlined here is that the Eq. (30) states that as the spectrum becomes more energetic (large steepness) and narrow, the kurtosis increases; therefore the probability of formation of a rogue wave increases as well. As mentioned before, this result is consistent with experimental results described in [88,89] and is the base for the operational forecasting (in a statistical sense) of rogue waves at the European Centre for Medium-Range Weather Forecasts (ECMWF) [103].

Effects of finite and shallow water have been discussed in [81]; in particular it has been shown that when $k_0h < 1.36$ the last term in (30) becomes negative, so that the kurtosis becomes less than 3. This has been confirmed numerically in [104]. Values of the kurtosis less than 3 have also been observed in numerical simulations [105] of the Korteweg de Vries equation that describes the dynamics of shallow water waves.

Ocean waves are not long crested and this is the main criticism to the theory developed. A correction to the Benjamin–Feir Index for short crested waves has been considered in [106,107] and will be discussed briefly in Section 6.

5.2. The contribution to deviations from Gaussian statistics by bound modes

The idea that deviations from Gaussian statistics of the surface elevation could result separately from a contribution of bound and free modes was first exploited in [108] and then followed in [43,109]. Indeed, it possible to estimate the skewness and the kurtosis from bound modes components. In the narrow band approximation, the calculation is straightforward for long crested waves: starting from the definition of the skewness and kurtosis and using Eq. (15) and averaging over the phases, one finds, respectively: (see [110,95]):

$$s = \frac{\langle \eta^3 \rangle}{\langle \eta^2 \rangle^{3/2}} = 3k_0\sqrt{\langle \eta^2 \rangle} \tag{31}$$

$$\kappa^{(bound)} = \frac{\langle \eta^4 \rangle}{\langle \eta^2 \rangle^2} = 3 + 18(k_0\sqrt{\langle \eta^2 \rangle})^2. \tag{32}$$

The bound modes contribution to the kurtosis is related to the steepness of the waves, therefore the dynamic contribution of the kurtosis (which depends also on the spectral bandwidth) can in principle be much larger than the one from the bound modes (at least for long crested waves). The effects of finite water depth on s and $\kappa^{(bound)}$ are discussed in [43].

In broad band (both in frequency and angle) spectra the effect of bound modes cannot be estimated analytically and numerical calculations are needed. The calculations are based on the model developed by Longuet-Higgins [111] and then re-considered in [112]. In principle, the model is able to include the effects of wave steepness, water depth, and directional spreading with no approximation other than the truncation of a small-amplitude expansion to the second order (resonances or quasi-resonances as the modulational instability are not contained in the model). Explorations of this method for short-crested waves (see, e.g., [113,114]) have shown that statistical properties of second-order simulated time series agree relatively well with many field measurements in both deep and intermediate water depth. In [115] the second-order surface wave model is used to investigate the effect of double peaked directional wave spectra at different water depths. For unimodal seas (i.e. single peaked), the addition of directional components reduces the effects of the second-order interactions in deep water and increases them in shallower depths. For a bimodal sea (i.e. double peaked), on the other hand, a large angle between the wave trains decreases systematically the vertical asymmetry of the wave profile. However, evident deviation of the wave crest distribution at low probability levels if compared with the unimodal condition are observed when two wave spectra are slightly separated in direction. In [116] the same second order model finite-depth wave theory is here used to investigate the statistical properties of the surface elevation and wave crests of field data from Lake George, Australia. By low-pass filtering the Lake George time series, there is evidence that some energetic wave groups are accompanied by a setup instead of a setdown (i.e. the long wave component is in phase with the wave group and not in anti-phase as predicted by Longuet-Higgins and Stewart [117]). A numerical study of the coupling coefficient of the second-order difference contribution predicts a setup as a result of the interaction of two waves with the same frequency but with different directions. This idea was exploited in [118] to explain the set-up observed in the famous Draupner data.

6. Rogue waves in two horizontal dimensions

Ocean waves are only rarely long crested and more often are characterized by a directional spectrum (see Eq. (8)), i.e. the energy is distributed in angle and not only in frequency. This has some consequences on the statistical properties of surface gravity waves and in particular on the formation of rogue waves. The issue was discussed for the first time in [119] from laboratory measurements and in [120] where numerical simulations in two horizontal dimensions of a higher order NLS equation have been performed. It has been shown that by increasing the directionality of the initial spectrum the appearance of deviation from Normal statistics is reduced. Those papers were then supported firstly in [121] and then by a much more detailed analysis in [122] where a large number of simulations have been performed to reveal how the occurrence of freak waves on deep water depends on the group and crest lengths for fixed steepness. It has been found that there is

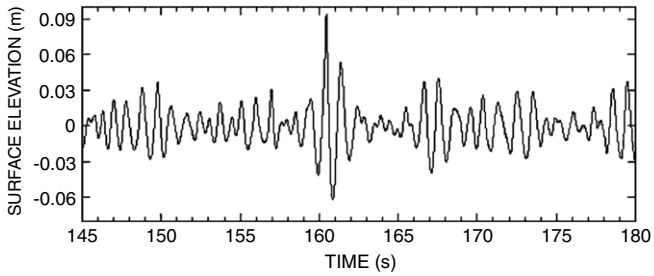

Fig. 18. Time series showing a rogue wave.
Source: From [8].

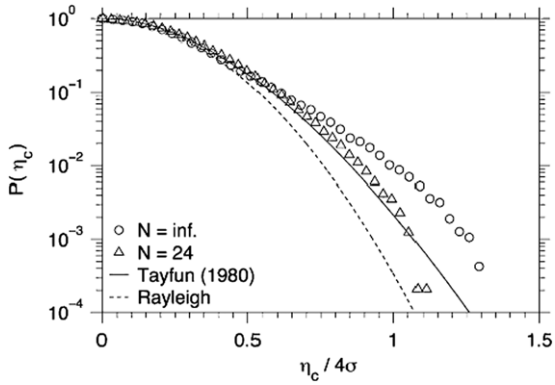

Fig. 19. Exceedence probability for wave crests estimated from time series recorded at the probe where the maximum of kurtosis is observed.
Source: From [8].

a sharp qualitative transition between short- and long-crested sea, for a crest length of approximately ten wavelengths. For short crest waves the statistics of freak waves deviates little from Gaussian. For long crest waves the statistics of freak waves is strongly non-Gaussian and the BFI is a good indicator of increased freak wave activity. Experimental verification of these results have been conducted independently in the Laboratories of the Tokyo University [123] and of the Marintek (Norway) [124]. The experiment in Japan was conducted in a facility 50 m long, 10 m wide, and 5 m deep with a segmented plunger type directional wave maker equipped with 32 plungers. The Marintek basin is one of the largest in the world; it is 50 m long and 70 m wide with an adjustable depth of 10 m maximum. The basin is equipped with a multi-flap generator composed by 144 flaps. Both basins are equipped with absorbing beaches at one end (opposite to the wave maker) in order to reduce wave reflections. The experiments consisted in generating a directional spectrum with random phases (see Eq. (8) and Figs. 1 and 2) at the wave maker and let the waves evolve along the tank. The experiments where conducted for different values of the directional parameter N. Even though the basins have different sizes and aspect ratios, the results in both experiments are consistent with each other [8]. In Fig. 18 a typical time series including a rogue wave is shown; it is also interesting to note the presence of a deep hole after the large wave. The height of the largest wave is about 2.5 times larger than the significant wave height. In Fig. 19 the probability of exceedence for wave crests normalized with 4 times the standard deviation is shown for $N = 24$ (short crested waves) and $N = \infty$ (long crested waves). The figure also includes the Rayleigh and the Tayfun [29] predictions. The latter is based on second order Stokes theory, therefore it accounts for bound modes up to second order. The statistics of short crested waves is well described by the Tayfun distribution, however for long crested waves the experimental data are well above the theoretical predictions. In Fig. 20 we show the evolution of the kurtosis along the wave tank for different values of N. Clearly larger values of N results in larger kurtosis. These experimental results have been confirmed also numerically [125] using both the envelope equation approach [126] and the Higher Order Spectral Method [127].

In [128] wave data from the Kvitebjorn platform (190 m deep) in the northern North Sea from 2003 to 2005 were analyzed. The data were used to select the days when relatively more freak waves were observed. The days were classified into freakish and non-freakish days, respectively. It was found that the freakish days are characterized by a directional spectrum that is in average 7.6° narrower in directions. This field experimental result support the idea that rogue waves appear more frequently in sea states characterized by a narrow directional spectrum.

Speaking in terms of equations, in one horizontal dimension the NLS has played a major role in the understanding of the main physical mechanisms of formation of rogue waves. An 2D version of the NLS equation can be derived from the Euler equations. However, such equation has some limitations: the instability region is unbounded and long time simulations leads to non-physical results (see [74]). The equation is not integrable and therefore analytical solutions, which have played

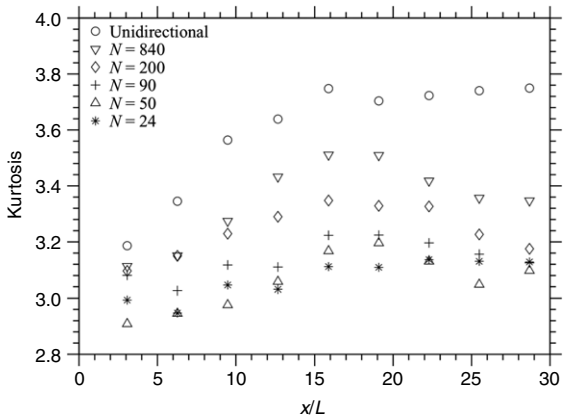

Fig. 20. Kurtosis as a function of distance from the wave maker for different values of N.
Source: From [27].

an important role in the one dimensional NLS (see Section 4.3), are lacking. As mentioned before higher order NLS equations have been used for numerical simulations [120–122]. A different numerical approach, not based on envelope equation has been devised in [129]. The simulations are based on fully nonlinear equations describing weakly three-dimensional potential flows of an ideal fluid with a free surface in terms of conformal variables [130,131]. Simulations are performed starting with a perturbed Stokes wave. Spontaneous formation of zigzag patterns for wave amplitude is observed in a nonlinear stage of the instability. If the initial wave steepness is sufficiently high a rogue wave is produced (see also [132]). In [133] it has also been shown that the maximum amplitude reached by the rogue wave is related to the angle between the perturbation and the original Stokes wave. This result can be easily understood in terms of the 2D NLS equation.

Because of the strong dependence of the statistics on the directional spreading the concept of the BFI, as defined for one dimensional wave propagation, is not suitable for operational forecasting of rogue waves. In [106] a modification of the BFI which include also the width of the spectrum in angle has been proposed. The work is mainly based on Monte Carlo simulations of the nonlinear Schrödinger equation in two horizontal dimensions. A large number of simulations have been performed in order to obtain the behavior of the kurtosis as a function of the BFI and directional spread in directional sea states. The parametrization of the dynamical kurtosis estimated from directional spectra is the following:

$$\kappa^{dyn} = 3 + \frac{\pi}{\sqrt{3}}\mathrm{BFI}_{2D}^2 \tag{33}$$

where the BFI_{2D} is the effective BFI parameter which includes directional effects. It is given by:

$$\mathrm{BFI}_{2D}^2 = \frac{\mathrm{BFI}^2}{1 + \frac{\alpha \Delta\theta^2}{2(\Delta\omega/\omega_0)^2}} \tag{34}$$

$\Delta\theta$ is measure of the angular width of the spectrum and $\alpha = 7.1$ is a fitting parameter; the error of the parametrization is at most 10%. The parametrization is verified against laboratory data, and good agreement is obtained, [106].

7. The role of inhomogeneity: the Alber–Saffman approach

As has been already made clear in the present review, one mechanism of formation of rogue waves is the modulational instability which formally is the result of the linear stability analysis of a monochromatic wave to side band perturbations. In real sea state conditions, the spectrum is characterized always by a finite width and the modulational stability analysis procedure cannot be adopted. Therefore, one should consider the problem of the stability of a wave spectrum to non-homogeneous perturbations. The methodology to accomplish such task has been developed in [134,135] and is based on a statistical description of the NLS equation. In the context of rogue waves such approach has been used in [41,136,137]. The idea is to start with the NLS equation (16) and apply the Wigner transform [138] defined as:

$$P(x, k, t) = \frac{1}{2\pi}\int_{-\infty}^{+\infty} \langle A^*(x + y/2, t)A(x - y/2, t)\rangle \exp[-iky]dy \tag{35}$$

and derive an evolution equation for the second order correlator $P(x, k, t)$, which is nothing but a wave spectrum that depends on the spatial coordinate x. After using the random phase approximation, a Vlasov–Poisson-type of equation is obtained and the linear stability of the spectrum can be worked out. In [136] the stability of a JONSWAP like spectrum (see Eq. (7) and Fig. 1) is investigated. The final result is the instability diagram reported in Fig. 21 where the (γ–α) plane is shown. We recall that γ is related to the width of the spectrum: the larger the value of γ is, the narrower the spectrum is. α is related

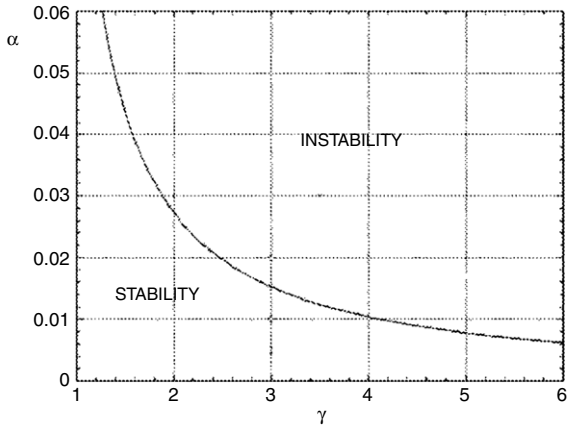

Fig. 21. Instability diagram in the (γ–α) plane.
Source: From [136].

to the total energy of the spectrum: large values of α indicates larger significant wave height and for fixed dominant wave number, it corresponds to larger steepness. The results indicate that the spectrum is unstable for large values of α and γ; this implies that in order to have instability the steepness must be large and the spectrum narrow banded. In [136] it has been shown that the instability of the spectrum corresponds to the formation of coherent structures which are probably of breathers type. Concerning the propagation in two horizontal dimensions, in [139] it has been showed that the stabilization only depends on the bandwidth of the wave vector component in the main propagation direction, and does not depend on the transversal direction (crest length). The Alber–Saffman approach has been used in [137] to study the interaction of wind waves and swell (wave propagating without the forcing of the wind) as a mechanism for the generation of rogue waves. They show that in such a sea state, the probability of freak waves higher than twice the significant wave height increases by a factor of up to 20 compared to the classical value given by Rayleigh's distribution.

8. Rogue waves in crossing seas

Ocean waves are generated by wind and for pure wind waves the spectrum is characterized by a single peak whose coordinates in Fourier space indicates the dominant period of the waves and the direction of the waves. When the wind stops, waves can still travel long distances; such wave system is called swell. It can happen that the swell enters into an ocean region where a storm is taking place and locally wind waves are generated; the result is that the wave spectrum is now characterized by two peaks: one for swell and one for wind sea. Two wave systems can also be generated in the case of rapidly turning wind, in this latter case, even if the waves propagate in different directions they may have similar frequencies.

From a theoretical point of view, such mixed sea state can be idealized as a system of Coupled Nonlinear Schrödinger, CNLS, equations, each describing the dynamics of each sea state [140]. In [141] the linear stability analysis of the CNLS equations have been performed and it have been speculated that the modulational instability in the system could be responsible for the formation of rogue waves. It has been shown that given a single unstable plane wave, the introduction of a second plane wave, propagating in a different direction, can result in an increase of the instability growth rates and enlargement of the instability region (see also [142]). In the last mentioned papers it has been noted that there is a critical angle between the two wave systems, $\theta_c \simeq 70.6^0$, at which the interaction changes features, making the systems with $\theta < \theta_c$ more unstable due to overlapping instability regions and forming rogue waves at shorter time scales (see also [143–145] where numerical computations of the CNLS equations and fully nonlinear equations describing weakly three-dimensional waves, have been performed). In [146] a detailed analysis of the coefficients of the CNLS equations have been performed and besides the growth rate of the perturbation, the maximal amplification factor of the unstable waves was considered. For $\theta \simeq 53.5^0$ the system CNLS becomes integrable and exact rogue wave solutions of the Peregrine type have been found [147]. The conclusions of the paper is that rogue waves is the result of a compromise between strong nonlinearity and large growth rate and it has been estimated that this happens for angles between 40^0 and 60^0. This result has been confirmed in an experimental work performed in the Marintek laboratories and in numerical computations [148].

It should be mentioned that an accident of a rogue wave that impacted on the cruise ship Louis Majesty in the Mediterranean see along the coast of Spain has happened in crossing sea conditions in March 2010; such event has been analyzed in details in [149].

An interesting idea on the generation of rogue waves has been proposed in [150] where the authors have analyzed an accident along the Japanese coast of a fishing boat. Some hours before the accident a wind sea and a swell coexisted. Under the influence of rising wind speed, the swell system grew exponentially at the expense of the wind sea energy, and the bimodal crossing sea state transformed into an unimodal sea state, characterized by a very narrow spectrum and

steep waves. This last condition is characterized by a large BFI and therefore suitable for formation of rogue waves *via* the modulational instability process.

9. Rogue waves and currents

It is has been known for many years that in the regions of the ocean where a current is present, "abnormal" waves have been observed (see [151]). The current changes the dispersion relation and may refract waves to converge in a single point creating a large amplitude wave (see [152] for an old but good review on the interaction of waves and current; more recent papers on the subject are [153,154,2,155–157]). It is well known that waves traveling in non-homogeneous currents may give rise to phenomena such as caustics formation. This phenomenon is well understood in terms of the linear theory of waves. Such mechanism is well described in [23] and will not be covered here.

In this section we will describe only recent developments on the formation of rogue waves in the presence of currents in weakly nonlinear wave fields. In [158] the combined effects of refraction and nonlinearity on the evolution of ocean surface wave statistics are considered and possible implications for the likelihood of rogue waves are examined. The authors derived a deterministic model that accounts for cubic nonlinear dynamics and weak lateral homogeneity of the medium. Through Monte Carlo simulations, the evolution of wave statistics in freely developing waves over an opposing shearing current are computed. The simulations show that freely developing, directionally spread wave fields generally maintain near-Gaussian statistics. However, the enhanced nonlinearity caused by the refractive focusing of narrowband wave fields can result locally in strongly non-Gaussian statistics.

In [159] the authors derive a modified 2DNLS equation which includes a slowly varying in space current; they investigated, using again Monte Carlo simulations, the effect of nonlinearity with respect to the variation of significant wave height, kurtosis and occurrence of freak waves. They showed that depending on the configuration of current and waves, the kurtosis and the probability of freak waves can either grow or decrease when the wave height increases due to linear refraction. They investigated a jet like current and found that at the center of the opposing current jet where waves are known to become large, freak waves should be more rare than in the open ocean away from currents. The largest amount of freak waves on an opposing current jet is found at the jet sides where the significant wave height is small. In [160] the author used the same model as derived in [159] and show that in one horizontal dimension the model can be reduced to an NLS equation with a non constant coefficient in front of the nonlinear term. The effect is that as the waves enter into an opposing current, the nonlinearity grow and rogue waves can be triggered naturally. The equation used in [159,160] has been criticized in [161] because it does not preserve wave action properly and a new modification of the NLS for variable currents has been proposed. However, the mechanism of triggering rogue waves in opposing current still work within such modified equation.

A current modified higher order envelope equation has also been used in [162]. They showed that when the average steepness is large the key variables determining the probability distribution are the steepness, and the angular and frequency spread of the incoming waves. Greater probability of extreme wave formation is predicted when linear focusing and nonlinear effects are acting together.

At this point, what is still lacking is a comparison between the model simulations and observations and experiments.

10. Rogue waves in other physical systems

Rogue waves in laboratory experiments are easier to investigate than ocean rogue waves because the experimental systems offer often the possibilities of handling the parameters that are at the origin of the extreme waves. At the same time, the collection of many events becomes possible in relatively short time intervals, depending on the typical response time of the system considered. For these reasons, there has been recently a considerable effort to study rogue waves in a number of different physical contexts. The experimental realizations include weak turbulence in superfluid Helium [163], transport in microwave systems [164], parametrically driven capillary waves [165], plasmas [61] and various optical systems [9,12]. On the other hand, numerical simulations have also been performed in different contexts and led to study rogue waves in a number of systems, for instance, in plasmas [166], Alfvén waves [167], Bose–Einstein condensates [168], discrete nonlinear lattices [169].

The aim of this section is to give a brief description of some of the above mentioned systems and of the associated rogue wave phenomena. In particular, we will focus on: the transient rogue waves appearing during the inverse cascade of the wave turbulence regime in superfluid Helium, the linear rogue waves resulting from the inhomogeneous emission of a large number of microwave antennas, the rogue waves occurring on the surface of a parametrically driven fluid and rogue waves in plasma systems. We have chosen these examples not only because they represent different physical systems but also because they are representative of different originating mechanisms.

The questions arising from the comparison of the different systems, their analogies and differences, bring forth the searching for an unified conceptual source of rogue waves, which is still a matter of debate. This debate is particularly active in the field of optics, where different approaches for the excitation, and the explanation, of optical rogue waves have been proposed, with some of them close to the classical description in terms of modulational instability and envelope solitons as solutions of the NLSE, and other closer to different approaches, as the wave turbulence theory [7] or the linear superposition of many uncorrelated waves [15]. Optical rogue waves will be presented more extensively in the next sections.

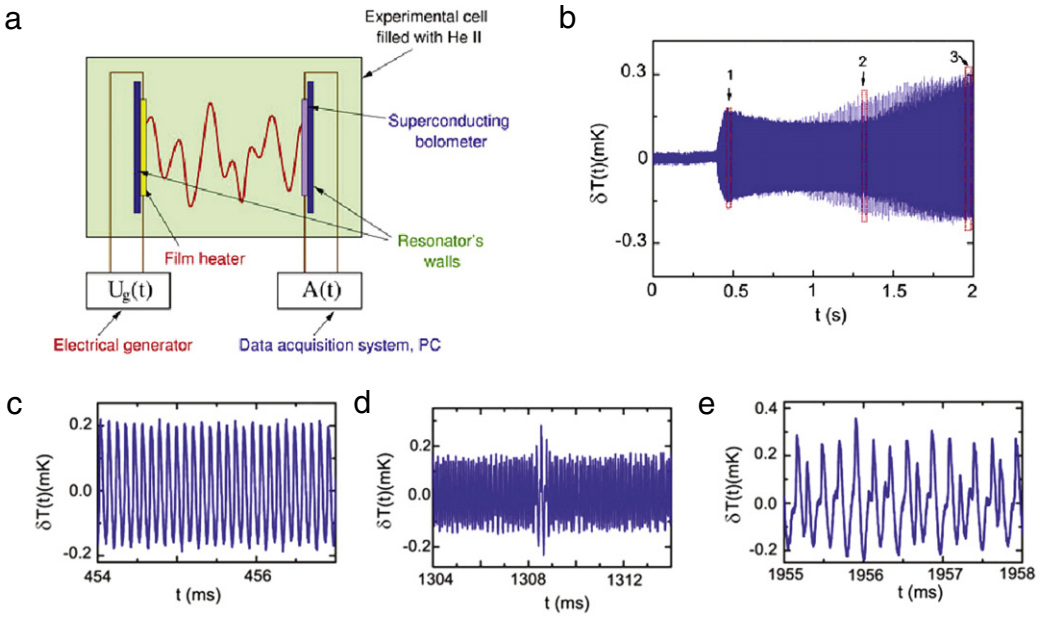

Fig. 22. (a) Experimental setup for the observation of second sound waves in superfluid Helium. (b) Evolution of the second sound wave amplitude after switching on the drive at a frequency near resonance; the signals (c)–(e) are enlarged plots corresponding to the 1–3 windows indicated by the arrows. Rogue waves appear in the 2 window and typically accompany the subharmonic formation that characterizes the inverse cascade.
Source: From [170].

10.1. Wave turbulence and rogue waves in superfluid Helium

When cooled below the critical temperature of $T_\lambda = 2.17$ K, ^{4}He condenses to form a liquid that has remarkably different properties than a normal fluid. It is, usually, called He II to distinguish it from the He I above T_λ. He II behaves as if it were a mixture of two different fluids: a normal fluid component with viscosity and carrying all of the thermal energy of the liquid, and an inviscid superfluid component with zero entropy. The two fluids separately fill the containing vessel.

Oscillatory counterflow of the two components can occur at constant density and pressure, corresponding to a temperature–entropy wave known as second sound. Second sound has a relatively low phase velocity (∼20 m/s) and an extremely small attenuation coefficient for frequencies below about 1 MHz. Its velocity u_2 depends strongly on its amplitude δT and can be approximated as

$$u_2 = u_{20}(1 + \alpha\delta T), \tag{36}$$

where u_{20} is the velocity at vanishingly small amplitude. The nonlinearity coefficient α can be made large, and either positive or negative, by adjustment of the temperature. The strength of the wave interactions is determined by α, hence, can be easily controlled. These properties make He II an ideal medium for systematic studies of nonlinear interactions between waves [163,170].

Rogue waves have been observed in an experiment involving second sound waves within a resonant cavity filled with superfluid Helium. Because of the small attenuation coefficient for the second sound, the quality factor of the cavity is very high, enabling large wave amplitudes to be achieved. Being a temperature wave, second sound can conveniently be excited with a heater and detected thermometrically. Energy is injected in the system by a thin heater sinusoidally driven by a harmonic voltage generator in the frequency range 0.1–100 kHz, while the frequency of the second sound (twice the frequency of the voltage generator) is set close to a longitudinal resonance of the cavity.

Under certain experimental conditions a direct energy cascade exists, that is, the energy injected at the driving frequency flows steadily towards higher frequencies with negligible dissipation until the viscous cut-off is reached, beyond which it is rapidly dissipated as heat. When the driving amplitude is increased or the detuning of the drive from the resonant frequency is decreased, an inverse cascade appears, which is associated with an instability against the formation of subharmonics. Rogue waves are observed during the transient evolution of the inverse cascade, that is, they accompany the subharmonic formation that characterizes the inverse cascade. A typical experimental evolution is shown in Fig. 22.

Rogue waves in superfluid Helium have, so far, only been observed during the transient evolution of the second sound waves, in the wave turbulence regime and while the inverse energy cascade is evolving. Their relation with rogue waves on the ocean surface include similarities: in both cases, the phenomena under consideration are non-equilibrium in nature, the rogue waves are rare, extreme, events and appear to arise from an instability of large amplitude waves. The differences

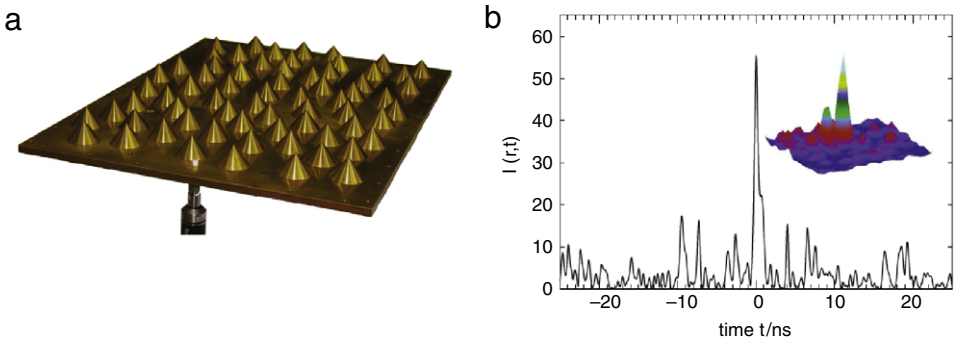

Fig. 23. (a) Experimental setup for the observation of rogue waves in a microwave system: the platform has width 260 mm and length 360 mm; the probe antenna is fixed in a horizontally movable top plate located 20 mm above the bottom (not shown). (b) A rogue wave event: the time evolution of wave intensity at the center of one of the hot spots is shown for the most extreme event observed; the inset shows the region surrounding the hot spot at the moment of the freak event.
Source: From [164].

include: the second sound waves are produced directly by a periodic driving force, whereas on the ocean roughly periodic waves are created by e.g. wind of a sufficient velocity, the second sound waves are one-dimensional standing waves, within the volume of the fluid, whereas the ocean waves are on the surface and can propagate in two dimensions, rogue waves on the ocean can apparently appear under steady state conditions, whereas those in second sound have only been observed during the transient evolution of the inverse energy cascade [170].

10.2. Microwave experiments: two-dimensional rogue waves in the linear regime

Rogue waves have recently been observed in a study of microwave transport [164]. The experimental setup, shown in Fig. 23a, is made of randomly placed metallic cones, each mimicking an r^{-2} potential on the scale of its radius. The metallic bottom plate supports the random arrangements of scatterers. The source antenna is mounted close to one of the short sides, and varying its position enables the incoming waves to arrive from different directions. The drain antenna is mounted in the top plate (not shown) and acts as a probe. The top plate can be moved in both horizontal directions, allowing for a spatial mapping of the wave fields within the scattering arrangement.

For wavelengths smaller than or comparable to the scatterer size (frequency $f = 30$–40 GHz), the system shows branching structures reminiscent of electron current distributions observed in two-dimensional electron systems [164]. At wavelengths larger than the cone size (frequency $f = 7.5$–15 GHz), the bulk of the intensity distribution approaches a multiple-scattering correction to Rayleigh statistics, as expected in multiple-scattering media. However, the probability of finding very high intensities is greatly enhanced with respect to the predictions provided by the Rayleigh statistics.

The extreme events in the microwave system occur in space (two-dimensions) and time, therefore, offering several qualitative analogies with the rogue waves on the ocean surfaces. However, the microwave system is linear, so that the origin of the extreme events cannot be searched in a modulational instability effect, as it occurs for nonlinear waves, and the description in terms of envelope solitons fails in this case. What is suggested by the authors is that the large deviations from the Rayleigh distribution is a consequence of inhomogeneities in the system and of averaging over different configurations of disorder. The randomly placed cones behaves like lens, which occasionally focus the microwaves into a hot spot (the mechanism is very similar to the focusing obtained by random currents [153]. Indeed, it is verified by fixing the probe position that the local distribution of intensities is a Rayleigh law $P_{loc}(I) = s^{-1}e^{-\frac{I}{s}}$, with the time-averaged value $s = \langle I \rangle$ depending on the chosen position. Then, the overall distribution of time-dependent intensities, collected over different positions and/or realizations of the disorder, is given by the integral of the local distributions, which yields a chi-square distribution that fits the experimental data.

This example shows how inhomogeneity can play a key role in inducing large deviations from the Gaussian wave statistics. As reported in the following section, such a key role of inhomogeneity has emerged also in optics, both in nonlinear [12] and linear experiments [15]. In particular, in the linear systems the inhomogeneity appears as an essential ingredient. Indeed, in this case the construction of the rogue wave events can be understood in terms of linear superposition of wave packets traveling with different group velocities and interfering constructively at a given space position and at a certain instant time. For this rare and positive coincidences to occur more frequently the spectrum of the possible group velocities must be large, a condition that is enhanced if the system is largely inhomogeneous.

10.3. Extreme events in parametrically driven capillary waves

Parametrically excited waves occurs at the surface of vibrated fluids as a consequence of the interplay between gravity and the capillary forces that tend to maintain the surface of the liquid at its rest position. Above a critical amplitude of

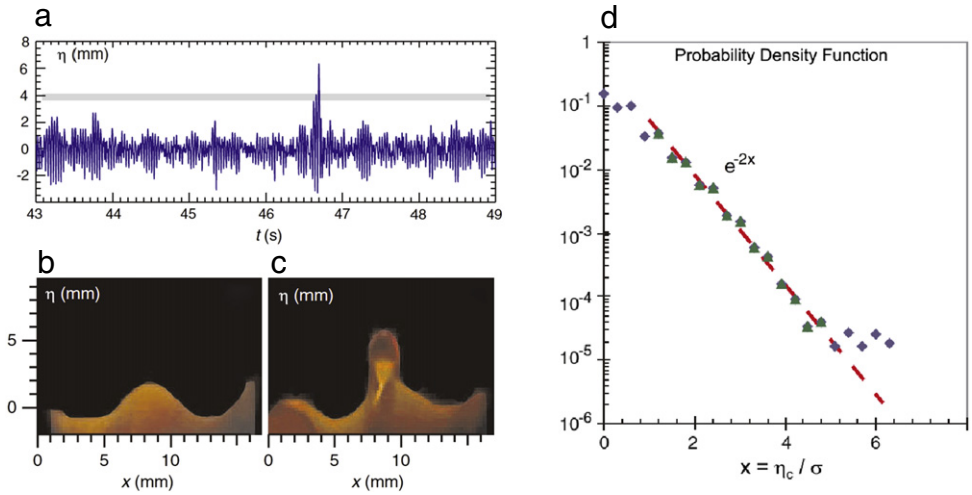

Fig. 24. (a) Time trace of the surface elevation showing an extreme wave event in parametrically driven capillary waves. Instantaneous snapshots showing waveforms: (b) 4 periods before the large event, and (c) during the large wave event. (d) Probability density function of the wave crests versus the normalized crest height.
Source: From [165].

the forcing, an instability takes place for which small surface deformations are amplified and waves oscillating at half the forcing frequency set on the surface of the vibrated liquid [171]. Capillary waves belong to the high frequency branch of the surface waves, for which the restoring force is the surface tension. Their wavelengths are typically shorter than about 10 mm. Because of their small scale, capillary waves can be studied under well-controlled conditions in the laboratory using a variety of experimental methods.

Extreme events have been recently obtained in a system of capillary waves excited parametrically in a vertically shaken container filled with water [165]. The waves were forced by shaking the container at the frequency of 60 Hz with an acceleration in the range of $a = 0.3$–5 g. The strength of forcing is characterized by the value of supercriticality above the threshold a_{th} of the parametric excitation, $\varepsilon = a - a_{th}$. The water surface was visualized by adding a small amount of a fluorescent dye to the water and by illuminating it with a thin green laser sheet. The motion of the fluorescent surface in the vertical cross section was then captured by a fast video camera.

Fig. 24a shows a time trace of the surface elevation $\eta(t)$ measured at the strongest forcing, $\varepsilon = 5$. This trace contains an extreme wave event, that is, a wave with a crest height >6 mm. The peak amplitude exceeds the standard deviation of the wave background by a factor of more than five. Two instantaneous snapshots show the waveforms before the peak, Fig. 24b, and during the large event, Fig. 24c. Note that the rogue wave is characterized by an almost vertical wave front.

Fig. 24d shows the probability density function of the normalized wave crest heights $x = \eta/\sigma$, where σ is the standard deviation, recorded for 300 s, or 104 wave periods. Strongest waves, $x > 5$, have a probability which is substantially higher than expected from the e^{-2x} Gaussian trend. The system displays, therefore, a statistical behavior typical of extreme events [172]. As for the frequency spectra of the parametrically excited waves, the development of frequency sidebands is first observed when the forcing is gradually increased, thus, suggesting that the classical phenomenology of modulation instability is, here, at the origin of the rogue wave phenomenon. Indeed, at further increase of the forcing the spectrum becomes continuously broadened and displays a triangular shape with exponential tails. Correspondingly, the PDF of the wave amplitude develops tails with crest heights in excess of 6.

The evolution of the wave amplitude in the time domain shows envelope solitons as a result of the modulational instability, and the nonlinear broadening of the spectra seems to originate from the generation of shorter envelope solitons, in analogy to the spectral broadening of the light pulses observed in photonic crystal fibers at the first stages of supercontinuum generation [173]. Then, the rogue wave generation in the parametrically excited waves probably results from a process similar to the collision of breathers as observed, for instance, in optical fibers [174]. In any case, modulation instability appears as a characteristic feature for the spectral broadening.

10.4. Rogue waves in plasmas

Numerical investigations have been, recently, reported for the generation of acoustic rogue waves in a dusty plasma composed of negatively charged dust grains and nonextensive electrons and ions [166]. A reductive perturbation technique has been used to obtain a nonlinear Schrödinger equation, hence, predicting a nonlinear evolution of modulationally unstable dust-acoustic wave packets. The authors show numerically that within the modulational instability region a random perturbation of the amplitude grows, thus, creating dust-acoustic rogue waves.

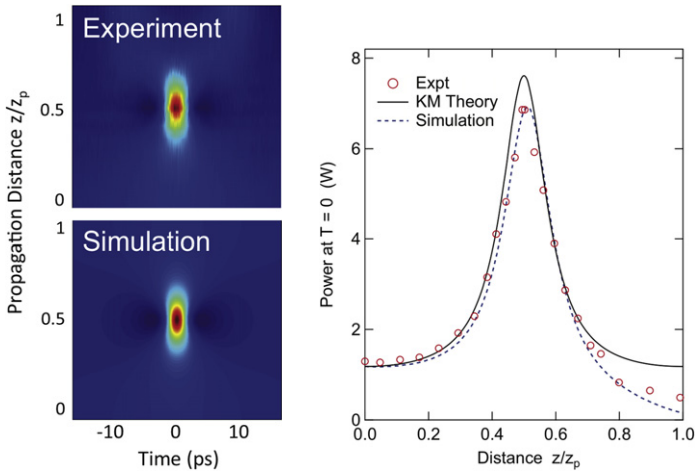

(a) Evolution of central lobe. (b) Power evolution with distance.

Fig. 25. (a) False color plot of experimental and theoretical intensity evolution with propagation distance. (b) plots the evolution of the power at the center of the modulation cycle as a function of normalized distance comparing experiment (red circles), the theoretical evolution of the KM soliton (black solid line) and simulation (blue dashed line). (For interpretation of the references to colour in this figure legend, the reader is referred to the web version of this article.)
Source: From [78].

Experiments in a multicomponent plasma with negative ions have, recently, reported the evidence of Peregrine solitons of ion-acoustic waves [61]. It is shown that, for a critical concentration of negative ions, slowly amplitude modulated perturbations undergo self- modulation, hence, giving rise to high amplitude localized pulses. The measured amplitude of the Peregrine soliton is 3 times the nearby carrier wave amplitude, which agrees with the theory and with the numerical solution of the nonlinear Schrödinger equation. Direct analogies for this type of soliton solutions can be established with the Peregrine solitons observed in wave tank experiments [59] and in optical fibers [60].

Finally, rogue waves, in the form of giant breathers, are numerically shown to develop in the Alfvén wave turbulence regime described by the randomly driven derivative nonlinear Schrödinger equation in the presence of a weak dissipation [167]. The distribution of the instantaneous global maxima of the Alfvén wave intensity fluctuations is shown to be accurately fitted by power laws, which contrasts with the integrable regime (absence of dissipation and forcing) where the behavior is rather exponential. As the dissipation is reduced, rogue waves form less frequently but reach larger amplitudes. Here, the rogue wave generating mechanism appears as related to a genuine wave turbulence regime. Analogies could be drawn with the rogue waves experimentally observed in the superfluid Helium during the wave turbulence inverse cascade [163].

11. Rogue waves in optics

We have witnessed, recently, a growing interest for rogue waves in the field of optics and lasers. This burst of investigation activities in the optics domain has been, firstly, triggered by the work of Jalali group [9], where the concept of optical rogue waves was introduced. There, high amplitude intensity peaks were identified in the supercontinuum generated by a nonlinear photonic crystal fiber. The high pulses, manifesting themselves in the intensity time series, are assimilated to the rogue waves observed on the ocean surfaces. Indeed, the light propagation in the nonlinear fiber can be described by a nonlinear Schrödinger equation and the high amplitude peaks occur close to the modulational instability regime, thus, establishing a direct analogy with the mechanism generating rogue waves in water waves [90]. However, the extreme waves observed in the optical fiber experiments are intrinsically of 1D nature, since they are peaks occurring during the temporal evolution of the light intensity. Moreover, the light intensity is usually measured as the spectral amplitude at a specific wavelength, or across a filtered spectral interval, of the whole emitted spectrum. Therefore, care must be taken when evaluating the statistical properties of such filtered intensity time series, because they can vary considerably when changing the filtering conditions [10].

Several works have followed [9] for studying optical rogue waves in the supercontinuum generation, comprising picosecond pulsed supercontinuum [10,175], continuous pumped supercontinuum [176] and femtosecond pulsed supercontinuum [177]. Envelope solitons have been experimentally identified in this context, in particular, the Peregrine soliton has been observed in nonlinear optical fibers [60] and more recently the Ma–Kuznetsov breather has also been reproduced experimentally [78]. In Fig. 25 we show the experimental results compared with the theoretical one, [78].

Optical rogue waves in the form of high peak temporal pulses have also been observed in fiber Raman amplifiers [178].

A different approach to optical rogue waves is proposed in [7], where the emergence of extreme events from wave turbulence regimes is demonstrated by numerical simulations of the nonlinear Schrödinger equation. Depending on the

amount of nonlinearity in the system (i.e. the ratio between the nonlinear part of the Hamiltonian to the linear one for the initial condition), three turbulent regimes that lead to the emergence of specific rogue wave events have been identified in [7]: (i) persistent and coherent rogue quasi-solitons, (ii) intermittent-like rogue quasi-solitons that appear and disappear erratically, and (iii) sporadic rogue waves events that emerge from turbulent fluctuations as bursts of light or intense flashes. We underline here that the ratio between the nonlinear and linear Hamiltonian is nothing but the BFI defined in Eq. (21) in the context of the NLS equation for water waves. The observation of high amplitude solitons is interpreted in view of establishing a link between the wave turbulence theory [179] and the rogue wave phenomena. The experimental verification of an optical wave turbulence regime has been reported for a one-dimensional in space liquid crystal system, where large amplitude solitons are, indeed, observed after the inverse cascade, when modulation instability of the wave condensate sets in [180,181]. However, a clear derivation of the rogue wave phenomenon from the soliton wave turbulence approach [182] still remains, up to now, not straightforward to achieve.

Because an unambiguous and widely accepted definition of rogue waves is still lacking, the debate on the possible classification of the different types of rogue waves is strongly interesting the scientific community, in particular, in the case of optical rogue waves, for which different examples and experimental systems are available. In order to clarify the issue, we can, at least, resort to the main phenomenological features that are common to rogue waves. First, rogue wave phenomena are characterized by large deviations of the wave amplitude statistics from the Gaussian behavior, the latter being typical of fully random systems. Another fundamental feature is that the emergence of high amplitude events must be the consequence of a coherent build-up that establishes itself during the propagation/interaction of many waves in an extended spatio-temporal system. In optical fibers the role of space is played by the frequency dispersion, hence, bringing forth a complex behavior in the time–frequency domain and leading to the appearance of coherent structures, or solitons, in the corresponding spectrograms. In spatially extended optical systems the wave dynamics occurs on the transverse wavefront and it is typically two-dimensional in space.

Then, despite the specificity of each experiment, other common properties that can be identified in rogue wave phenomena are related to the so-called "granularity" and "inhomogeneity", that is, rogue wave systems are usually characterized by the presence of many uncorrelated "grains" of activity, these being inhomogeneously distributed in larger spatial domains. Depending on the system under study and on the nature of the waves considered, grains can be of a different origin, for instance, solitons in nonlinear systems or wave packets in linear propagating waves, and their clustering in spatial domains can occur via different mechanisms, as a temporal delay, a spatial symmetry breaking, a transport phenomenon or a hypercycle type amplification [12].

In any case, rogue waves must be described by partial differential equations, because they intrinsically originate from propagation and dispersion, the latter being either temporal dispersion, as in optical fibers or in multimode lasers, or diffraction, as in spatially extended systems. In other words, it is essential, first, to have waves, hence, a dispersion relation, then, to let the system be able to introduce individual wave frequency changes, due either to dispersion or to nonlinearity, and finally to have a coherent build-up from the mistuned waves, such a build-up spontaneously occurring in certain space/time locations. Other types of spiking phenomena, observed, for instance, in certain laser systems, stem from different processes, as one dimensional chaotic behaviors [183] or noise induced intermittency [184], which are, indeed, described by ordinary equations. These processes do not belong to the class of phenomena that go under a wave-type description and must, therefore, be discarded from the rogue wave classification.

12. Optical rogue waves in fiber supercontinuum generation

In [9] optical rogue waves are identified as high amplitude peaks in the intensity time series of the light at the output of a nonlinear optical fiber. The experimental setup comprises a picosecond seed light pulse, at 1064 nm wavelength, propagating through a highly nonlinear microstructured optical fiber, a system known to generate supercontinuum radiation [173], that is, at the exit of the fiber the emitted light has a broad spectral contents, going from violet to red. By a particular type of filtering, only a small portion of the red spectral contents of the output field is kept (1450 nm). The amplitude evolution of the filtered intensity is recorded by a photodiode and plotted as a function of time. The time series are characterized by rare giant peaks over a noisy background, the number of the extreme events increasing when increasing the average power level of the input light. Three representative time series and corresponding intensity histograms are displayed in Fig. 26 for increasing values of the input intensity.

The L shape of the intensity histograms shows clearly large deviations from the Gaussian behavior, these deviations increasing at larger input powers. A nice analogy between the optical rogue waves and the ocean rogue waves is established on the basis of a common theoretical approach. Indeed, the supercontinuum generation in the photonic crystal fiber can be described by a generalized nonlinear Schrödinger equation, sharing several features with the NLSE describing the ocean surface. In the nonlinear optical fiber equation, dispersive terms plus nonlinearity ensure wave propagation phenomena and modulational instability, in analogy to what happens in water waves. Envelope solitons result from the modulational instability and appear in the time–frequency domain. There, they give rise to rogue waves through the ejection during the propagation from the pulsed temporal shape of the pump [10]. A representation of this process in displayed Fig. 27.

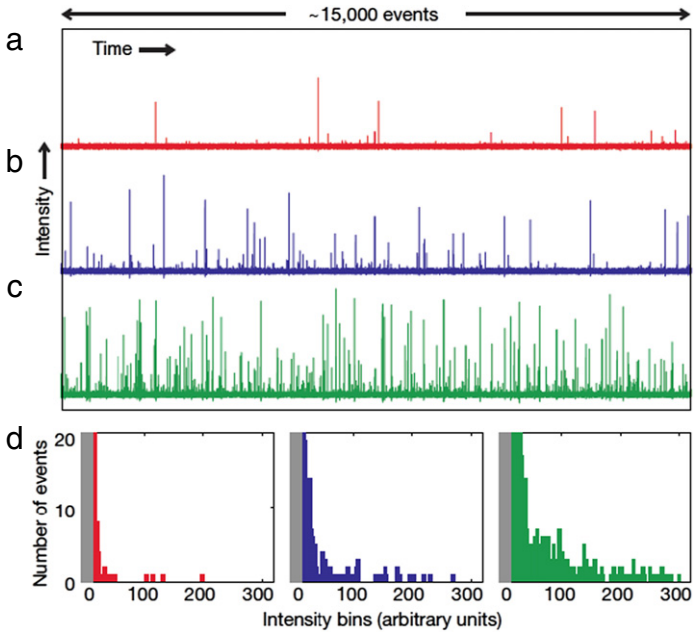

Fig. 26. Optical rogue waves in the supercontinuum generated by a photonic crystal fiber. (a)–(c) Single-shot time traces and (d) associated histograms for average power levels 0.8 mW (a and d-left), 3.2 mW (b and d-center) and 12.8 mW (c and d-right), respectively.
Source: From [9].

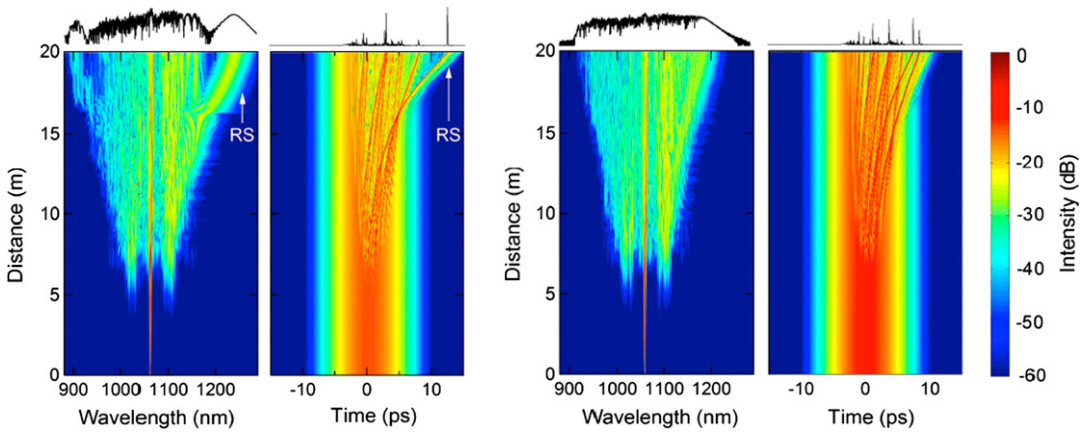

(a) Evolution of "rogue" event. (b) Evolution of "median" event.

Fig. 27. Rogue waves in the supercontinuum generation. Numerical spectrograms showing (a) the evolution of a rogue event generated by the emission of a high peak soliton around 1240 nm; (b) the evolution for a case where the output spectrum is closer to the distribution median.
Source: From [10].

12.1. The 1D generalized nonlinear Schrödinger equation

A generalized nonlinear Schrödinger equation is used to model the light propagation in the nonlinear optical fiber. The model equation reads as

$$\frac{\partial A}{\partial z} - \sum_{k\geq 2} \frac{i^{k+1}}{k!}\beta_k \frac{\partial^k A}{\partial t^k} = i\gamma\left(1 + i\tau\frac{\partial}{\partial t}\right)\left(A(z,t)\int_{-\infty}^{+\infty} R(t')|A(z,t-t')|^2 dt'\right), \tag{37}$$

where $A(z,t)$ is the envelope of the optical field and the β_k and γ are the usual dispersion and nonlinear coefficients. The nonlinear response $R(t) = (1-f_R)\delta(t) + f_R h_R(t)$ includes instantaneous and Raman contributions. The self-steepening timescale τ includes the dispersion of the nonlinearity due to the frequency-dependent fiber mode area.

The above equation has been used to perform numerical simulations. Harnessing and control of optical rogue waves has been proposed by a detailed numerical study of the evolution dynamics of statistically-rare extreme red-shifted soliton pulses arising from the supercontinuum generation [10].

12.1.1. Numerical simulations

Numerical simulations show that the rogue wave dynamics can be controlled by acting on the different system parameters [10]; it is shown that the generation of rogue waves can be enhanced by adding a small modulation to the input pulse envelope, whereas it can suppressed through the use of a sliding frequency filter. By plotting the field amplitude in the frequency and the time domain, rogue waves appear as soliton pulses that are red-shifted in the spectrum and propagates along the fiber. Numerical spectrograms showing the formation of rogue waves from the soliton emission are reported in Fig. 27.

12.1.2. Statistical properties

As for their statistical properties, it is shown that the optical rogue waves display a distribution well fitted by the Weibull function, a class of extreme value probability density functions, showing clearly a non-Gaussian behavior [10]. The Weibull function reads as

$$f(x) = C\left(\frac{x - x_0}{l}\right)^{k-1} e^{-\left(\frac{x-x_0}{l}\right)^k}, \tag{38}$$

where k, l and x_0 are shape, scale and location parameters, respectively, and C is the normalization constant. The shape parameter k characterizes the skewness of the distribution.

A detailed statistical analysis is performed in [185], where the PDF obtained in the filtered and unfiltered data are compared. There, it is shown that the statistics is largely modified depending on the filtering process applied to the light intensity data. This procedure eventually excludes the large events and leads to a more careful identification of classes of filtered and unfiltered optical rogue waves.

Interpretations on the origin of the optical rogue waves generated in fiber supercontinuum are proposed, which relay on the onset of convective modulational instabilities [176]. The convective nature of the rogue wave phenomenon is described by adding in the model higher-order terms (odd-order dispersion and stimulated Raman scattering) that break the time reversal symmetry of the nonlinear Schrödinger equation. It is shown that the third-order dispersion term alone turns the system to be convectively unstable, resulting in more powerful rare events. When, in addition, stimulated Raman scattering is considered, both the convective instabilities and the power of extreme events are further enhanced, giving rise to a probability density function with a more pronounced large tails.

12.2. Optical rogue waves in continuous pumped supercontinuum

Successive experimental works on nonlinear optical fibers have evidenced the appearance of rogue waves in correspondence with the soliton collisions that characterize the complex dynamics in the spectrograms, i.e. time–frequency plots, of the light intensity [175]. In [175] the photonic crystal fiber is pumped by a continuous (CW) laser. The CW-pumped supercontinuum exhibits optical rogue waves in analogy with the pulsed supercontinuum. However, in the continuous case the rogue waves result from temporal collisions among a gas of solitons, while in the case of pulsed pumping the rogue waves correspond to intense solitons that are ejected during the propagation from the pulsed temporal shape of the pump [10].

As for the statistics, the powerful and rare temporal events exhibit an L-shaped distribution. However, in logarithmic scale, the evolution of the PDF is quasi-linear, indicating a quasi-exponential behavior, therefore a quasi-Gaussian behavior. In pulsed pumping schemes, the rare events show quite different statistical properties, with large deviations from the Gaussian behavior. Indeed, despite the similarities of the experimental setups and of the qualitative observations in the intensity time series, the mechanism at the origin of rogue waves in the pulsed and CW pumped supercontinuum is drastically different. As pointed out in [175], while in the pulsed supercontinuum rogue waves are giant solitons that are ejected from the pump packet, in the CW pumping scheme, the rogue waves come from the collision of two propagating intense solitons. The latter mechanism is represented in Fig. 28.

Numerical simulations show the temporal evolution of spectrograms, that is, time–frequency plots, where the collision of two solitons can be identified as the phenomenon at the origin of rogue wave formation. Indeed, the two solitons, initially well separated in the time domain, travel at different group velocities because of their different spectral locations. Consequently, they become closer and closer in the time domain, until they collide and, after the collision, they again behave independently. The most interesting aspect of this process is the formation of a localized powerful spike, with a peak power 3–4 times higher than the mean power, which appears during the collision and disappears quickly just after.

12.3. Optical rogue waves in femtosecond pumped supercontinuum

The generation of optical rogue waves in supercontinuum has also been studied in the femtosecond pulsed regime [177]. The intensity histograms obtained from spectrally filtering the super-continuum exhibit the L-shaped characteristics typical

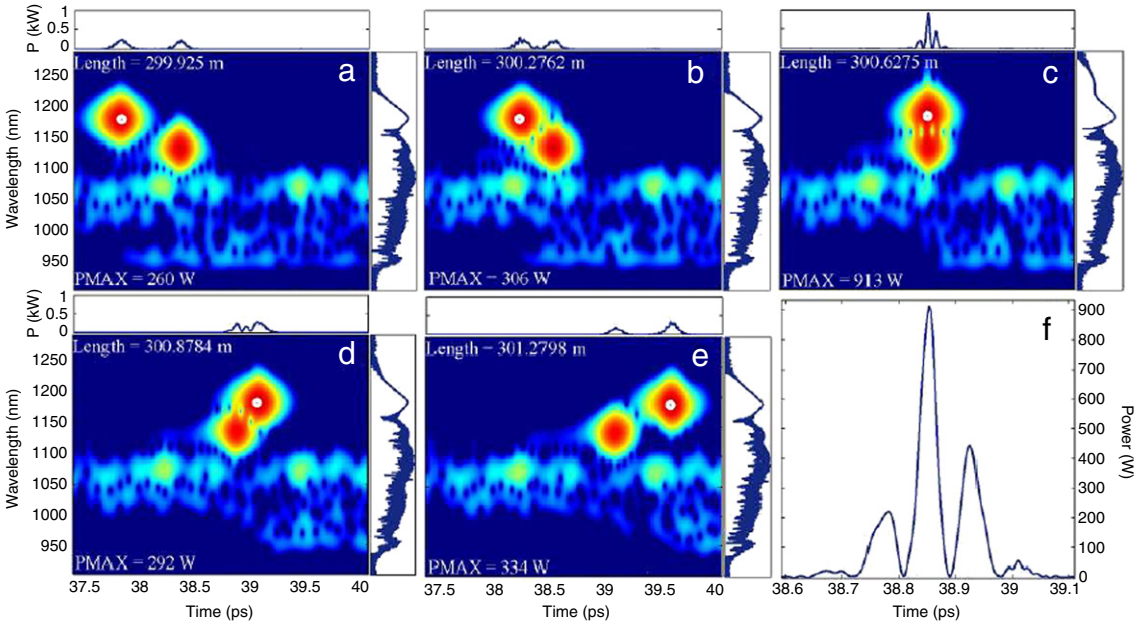

Fig. 28. Rogue waves are generated by soliton collisions in the time–frequency domain of the continuous pumped supercontinuum generation. (a)–(e) Single images displaying a close-up of the numerical spectrogram highlighting the collision between two solitons from $L = 300$ m to $L = 303$ m. (f) Power distribution in the temporal domain at the exact moment of collision.
Source: From [175].

of extreme value phenomena on both the long and short wavelength edges of the spectrum. The generation of rogue events is attributed to cross-phase modulation and soliton-dispersive wave coupling. Furthermore, the form of the histogram varies from L-shaped to quasi-Gaussian as wavelengths closer to the pump are included in the filtered measurements.

12.4. Rogue waves in Raman fiber amplifiers

Another class of optical rogue waves is identified by the extreme events observed in fiber Raman amplifiers [178]. By exploiting Raman amplification with an incoherent pump in nonlinear optical fibers, it is shown that the amplified signal develop a series of temporal intensity spikes whose peak power follows a long-tailed probability distribution.

In this context, the potential role of rogue waves in telecommunication data stream has been outlined in a recent theoretical study, where it is shown that the large broadening of short optical pulses due to fiber dispersion leads to a strong overlap in information data streams resulting in statistical deviations of the local power from its average [186]. The origin of the rare events examined here is linear, but the statistics of the high amplitude peaks deviate from the Gaussian behavior.

As for the origin of the extreme events in Raman fiber laser, a recent numerical study suggests that the mechanism of rogue wave generation in this kind of systems can be related to a turbulent-like four-wave mixing of the numerous longitudinal modes excited in the fiber [187].

12.4.1. Mode-locked lasers

Another approach to optical rogue waves in the temporal domain is that provided by a recent numerical work on mode-locked laser [188]. At difference with the conservative fiber systems that are described by a nonlinear Schrödinger equation, it is considered, here, the dissipative case of mode-locked lasers where the optical field propagates in a cavity in which gain is supplied in order to overcome the losses.

The system considered is a ring cavity that is composed of a nonlinear (Erbium doped) fiber, a single-mode fiber and a saturable absorber. The light field evolution is described by a set of partial differential equations that accounts for gain and losses in the cavity. Parameters can be chosen in such a way that the laser operates in the continuous regime or generates pulses, either a single stationary pulse or periodically oscillating pulses or a chaotic field with several pulses per round trip. Extreme events appear in the last situation, where the multi-mode dynamics taking place in the laser enables the constructive build-up of high intensity waves.

Other optical systems that are proposed as source of rogue waves deal with optical spiking that occurs, for instance, in lasers with injected signal because of homoclinic chaos dynamics [183] or in multistable lasers because of noise driven on–off intermittency [184]. In both cases, the respective mechanism of spiking is well-known (see, e.g., [189] for deterministic chaos in lasers with injected signal and, e.g., [190] for noise driven on-off intermittency). The recent identification of such pulsing

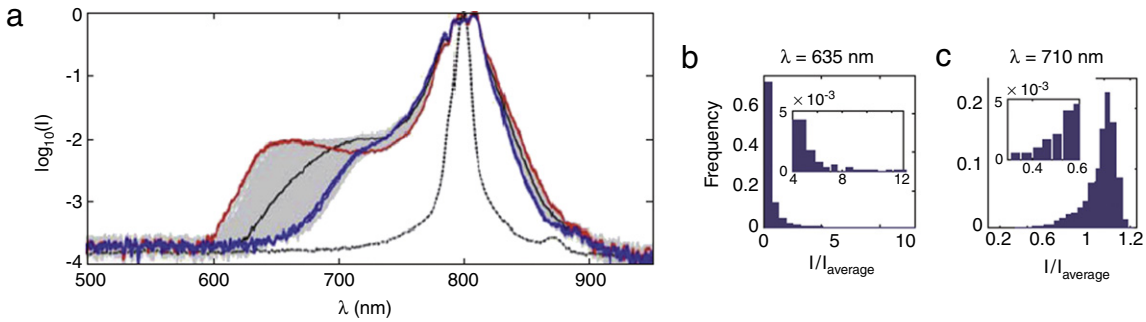

Fig. 29. Rogue waves generated by femtosecond filamentation. (a) Measured single-shot spectra of the filament (gray curves), the average spectrum is shown by the central (black) curve, the widest and the narrowest extremes are highlighted by the left (red) and right (blue) curves, respectively, while the input spectrum is plotted by the dashed curve. PDF of the spectral intensity at (b) 635 nm and (c) 710 nm. Insets show a magnified portion of the long tails. (For interpretation of the references to colour in this figure legend, the reader is referred to the web version of this article.)
Source: From [192].

behavior with optical rogue waves seems rather arbitrary because both systems are described by ordinary differential equations that do not admit a wave description (no dispersion relation).

13. Optical rogue waves in femtosecond filamentation

Another class of optical rogue events occur in femtosecond filamentation [191,192]. A high energy femtosecond pulse propagates either in a bulk medium, such as air, water or a crystal plate. In Ref. [191] optical rogue wave statistics is observed during high power femtosecond pulse filamentation in air. The wavelength-dependent intensity fluctuations is analyzed across 300 nm broadband filament spectra. While the statistics is nearly Gaussian in the vicinity of the pump, it becomes long tailed at the short wavelength and long wavelength edges of the spectra. The results are interpreted in terms of pump noise transfer via self-phase modulation.

In Ref. [192] a 130-fs pulse at $\lambda_0 = 800$ nm is tightly focused at the input face of a 43-mm-long cuvette filled with water. The input energy was chosen so as to excite a single filament, whose occurrence was verified by the white-light spectrum at the exit of the nonlinear medium. The statistical distribution of the spectral intensity reveal a non-Gaussian behavior, with long tails corresponding to rogue events observed at the edges of the spectra. The spectra and corresponding PDF of the intensity are shown in Fig. 29. In these experiments the longitudinal direction of light propagation leads to a strong space–time coupling and the observed rogue events are associated to X-wave formation in the normal group-velocity-dispersion regime, at difference with the temporal solitons observed in the anomalous regime in optical fibers.

A similar phenomenon is the white-light generation in thin bulk media, where the threshold for white-light generation almost coincides with the threshold for self-focusing and filamentation [193]. In the paper by Majus and coauthors [193] a statistical study of the white-light continuum generation in a sapphire plate is performed. The white-light continuum is generated by focusing a 130 fs pulse, 800 nm central wavelength, onto the input face of 3 mm thick sapphire plate. By analyzing the spectrum of the generated light, it is shown that, in certain input-pulse energy interval, the blue-shifted spectral components exhibit large intensity variations, with high peaks that obey a non-Gaussian statistical distributions. The PDF is quantified by using a Weibull fit function.

14. Optical rogue waves in 2D spatially extended systems

Rogue waves in 2D spatially extended optical systems have been studied in a nonlinear optical cavity [194]. In this system, rogue waves appear as high amplitude pulses that spontaneously build up on the transverse profile of the beam circulating in the cavity, where the non-Gaussian character of the wave amplitude statistics has been demonstrated [12]. Later, a linear propagation experiment has been setup, where light propagates in a multimode optical fiber. There, extreme events appear as a consequence of interference effects between the many waves propagating in the fiber [15].

A comparison between the nonlinear and linear setups has been very fruitful in view of identifying two key ingredients for the generation of optical rogue waves, namely, granularity and inhomogeneity. While granularity is a minimal size of the individual light spots, inhomogeneity is due to clustering of the light spots (grains) into separate domains characterized by different average intensities. In the nonlinear cavity, grains results from nonlinearity, which selects the typical space scale of field filamentation, while in the linear case grains are the consequence of multiple interference effects between the many modes propagating in the fiber. A symmetry breaking, introduced in the nonlinear cavity by an inversion of the return field and in the optical fiber by a tilt of the input wave vectors, ensures the inhomogeneous clustering of the grains. On the other hand, while dynamics is spontaneous in the nonlinear cavity, in the linear experiment it is introduced by appropriate external perturbations, adjourning the field distribution at the exit of the fiber.

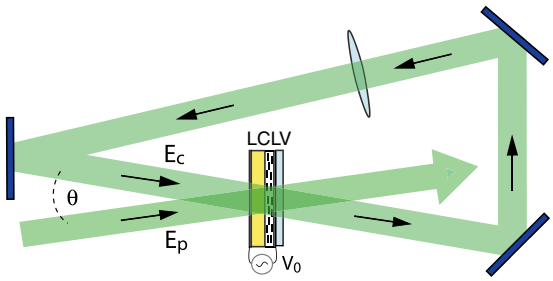

Fig. 30. A schematic illustration of the nonlinear optical cavity. The liquid crystal light-valve, LCLV, provides gain through wave mixing with the pump beam E_p, hence, leading to the spontaneous generation of the cavity field E_c.

In both case, the PDF of the intensity shows a non-Gaussian behavior, with large tails deviating from the exponential. Moreover, for the linear system it has been shown that the statistics of the waiting times between successive rogue waves occurring at the same space position follows a log-Poisson distribution [15]. This behavior is characteristics of temporal separation between large events occurring in cooperative and complex systems, with several examples arising in different fields, as geophysics and biology.

14.1. Nonlinear optical cavity

A nonlinear optical cavity is built by using a two-wave mixing process as a gain mechanism. The nonlinear medium is a liquid crystal light-valve, LCLV, a device formed by the assembly of a nematic liquid crystal layer with a photoconductive crystal [195,196]. An external voltage V_0 (typically of 20 V r.m.s. amplitude and with a frequency of 75 Hz) is applied across the cell, whereas the photoconductive substrate transfers it to the liquid crystal layer, within which occurs the wave-mixing.

When two light beams are sent to interfere on the LCLV, a fringe intensity pattern is created on the photoconductor, which, on its turn, generates a refractive index grating through the reorientation of the liquid crystal molecules. The two beams are, therefore, diffracted by the grating and, in undergoing this process, they mix-up, in the sense that part of the photons of one beam are diffracted on the direction of the other and vice versa. If one of the two beams, called the pump beam, is much more intense than the other, then, the wave-mixing provides a gain mechanism by transferring photons from the pump into the direction of the weak beam.

The nonlinear optical cavity reported in [194] is a ring formed by three high-reflectivity dielectric mirrors and a lens of $f = 70$ cm focal length, as illustrated in Fig. 30. The total cavity length is $L = 273.3$ cm and the lens is positioned at a distance $L_1 = 88.1$ cm from the entrance plane of the LCLV. The coordinate system is taken such that z is along the cavity axis and x, y are on the transverse plane.

The pump beam, E_p, illuminating the LCLV is an enlarged and collimated (10 mm diameter) beam from a solid state diode pumped laser ($\lambda = 532$ nm), linearly polarized in the same direction of the liquid crystal nematic director. Oscillations in the cavity are built from the wave-mixing in the LCLV. The gain is provided by wave-mixing with the pump E_p, and the cavity field E_c is spontaneously generated starting from the amplification of refractive index fluctuations in the liquid crystals.

Cavity field oscillations occur in a large range of parameter space, with V_0, the voltage applied to the LCLV, and $I_p = |E_p|^2$, the pump intensity, the control parameters [194]. Gauss–Laguerre modes are observed at the boundaries of the oscillation region, with the order and number of modes increasing as increasing V_0. A similar behavior is observed by fixing V_0 and then increasing the Fresnel number of the cavity, which is defined as the ratio of the area a^2 of the most limiting aperture, the transverse size of the LCLV in this case, to the size $w_0^2 = \lambda L$ of the fundamental Gaussian mode, $F = a^2/\lambda L$. The maximum number of transverse modes hosted in the cavity scales as F^2, F being the maximum number of nodes that fits the transverse size along one direction [197]. In the typical experimental conditions $F \sim 100$ and the number of cavity modes is as high as $F^2 \sim 10^4$.

For high F, many modes oscillates simultaneously in the cavity, giving rise to a speckles like behavior of the field. In this situation, extreme events appear as anomalous waves of large amplitude over the lower amplitude and fluctuating background. These optical rogue waves occur erratically in space and time, and live for a typical time of the same order of the response time of the LCLV. A typical experimental recording of such spatio-temporal pulses is displayed in Fig. 31.

14.2. The stretched exponential statistics

The optical rogue wave phenomenon is characterized by measuring the probability density functions, PDF, of the light intensity in the high F regime. The PDF are determined by acquiring a large set of images (about 1000) and then performing the histograms of the intensity values on the whole image stack. At this purpose, a small fraction (4%) of the field circulating in the cavity is extracted by a beam sampler and sent to a CCD camera (1024×768 pixels and 12 bits depth).

While for relatively low pump intensity, $I_p = 2$ mW/cm^2, the cavity field shows a complex spatiotemporal dynamics, with the formation of many uncorrelated domains, at larger pump extreme events, rogue waves, appear as large amplitude

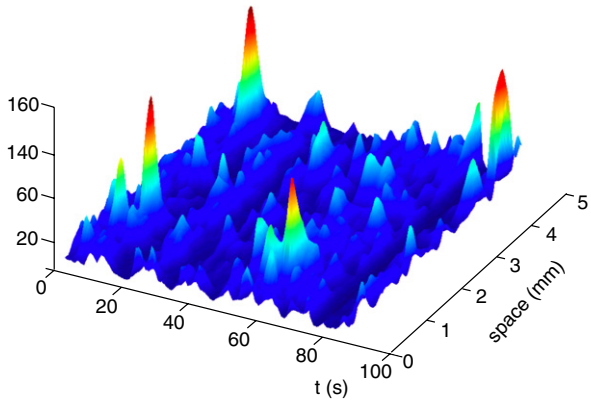

Fig. 31. Spatiotemporal pulses observed on the transverse profile of the light field circulating in the cavity.
Source: From Ref. [194].

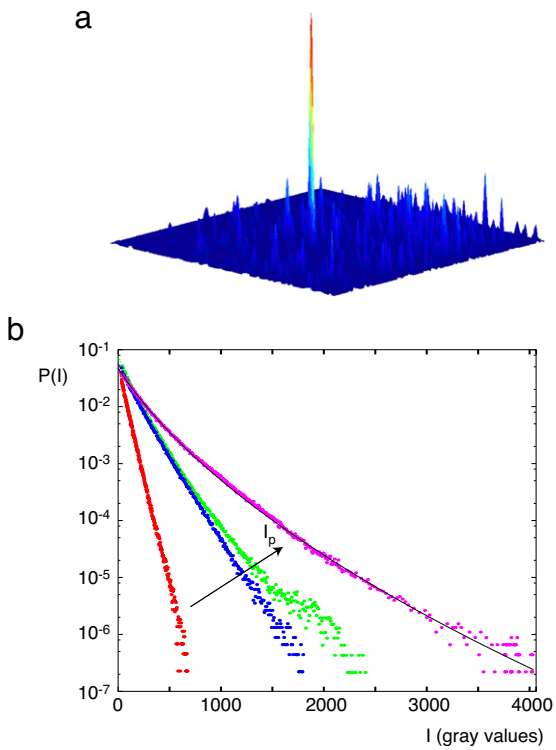

Fig. 32. (a) Instantaneous experimental profile of the transverse intensity distribution; an extreme event appears over a speckle-like background; (b) experimental PDF of the cavity field intensity; the pump is varied from $I_p/I_{th} = 1.8$, 4.0, 4.2, and 6.4 from the steepest to the shallowest distribution. The steepest distribution is exponential. The solid black line is the stretched exponential function that fits the shallowest distribution, with $c_1 = 29.5$.
Source: (From Ref. [12]).

peaks. An instantaneous experimental profile showing the transverse intensity distribution recorded for $I_p = 4.2$ mW/cm^2 is shown in Fig. 32a. A large event in the form of a high amplitude peak can be clearly distinguished. The optical rogue waves evolve spontaneously in space and time, appearing randomly and with a small probability. The typical time scale of the dynamical evolution is 100 ms, which is ruled by the response time of the liquid crystals [198].

In Fig. 32b the PDF of the cavity field intensity, $I = |E_c|^2$, are displayed for different values of the pump, $I_p/I_{th} = 1.8, 4.0, 4.2$, and 6.4, where $I_{th} = 1.2$ mW/cm^2 is the threshold for the optical oscillations to start in the cavity. The resulting PDF are plotted in log-linear scale, as shown in Fig. 32b. Increasingly large deviations from the exponential behavior are observed as the pump intensity is increased. All the distributions are well fitted by the stretched exponential function $Ne^{-\sqrt{c_1+c_2 I}}$, where $1/c_1$ is a parameter that measures the deviation from the exponential behavior. The black line is the fitting function of the PDF with $I_p/I_{th} = 6.4$.

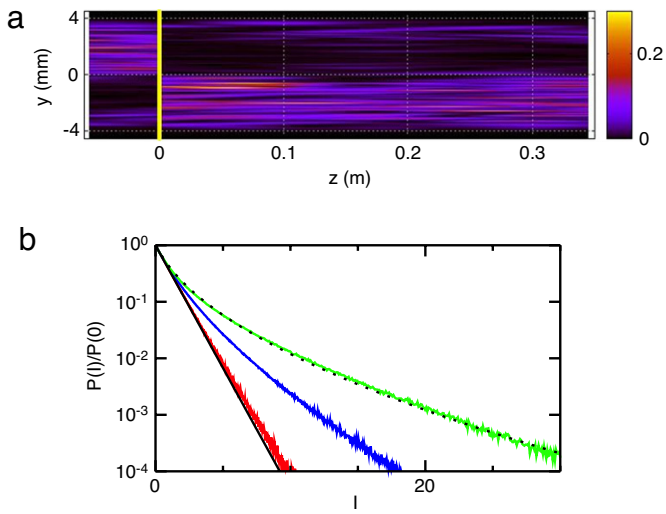

Fig. 33. (a) Cavity field intensity in the y-z plane; the yellow vertical line indicates the position of the LCLV; $I_p = 10$, $1 - \Gamma = 0.7$. (b) Numerical PDF of the cavity field intensity for different values of the pump $I_p/I_{th} = 6$ (steepest (red) curve), 8 (middle (blue) curve), 10 (shallowest (green) curve); $1 - \Gamma = 0.7$. The solid black line is a fit with an exponential; the dotted black line is a fit with a stretched exponential, $c_1 = 3.73$. (For interpretation of the references to colour in this figure legend, the reader is referred to the web version of this article.)
Source: From Ref. [12].

Note that an exponential statistics for the intensity corresponds to a Gaussian statistics for the field amplitude. Therefore, an exponential PDF of the intensity is characteristic of a speckles pattern, where each point receives the uncorrelated contributions of many uncoupled modes. At low pump, indeed, this is the behavior displayed by the cavity field. However, when the pump increases, the increasing nonlinear coupling leads to a complex space–time dynamics and extreme events populate the tails of the PDF, providing a large deviation from Gaussianity.

Because of the geometry of the cavity, which is formed by three mirrors in a quasi-spherical configuration, the field returning to the LCLV after a round trip is inverted along the transverse y axis. As a consequence, the nonlocal coupling of the cavity field E_c induces a dynamical symmetry breaking.

Numerical simulations have been performed by using the full model equations of the cavity, as described in [199]

$$\begin{aligned} \frac{\partial n_0}{\partial t} &= -n_0 + \alpha |E_c|^2, \\ \frac{\partial n_1}{\partial t} &= -n_1 + \alpha E_c E_p^*, \end{aligned} \tag{39}$$

where n_0 and n_1 are, respectively, the amplitude of the homogeneous refractive index and the amplitude of the refractive index grating at the spatial frequency $k_c - k_p$, k_c and k_p being the optical wave numbers of the pump and cavity field. α is the nonlinear coefficient of the LCLV, and the diffusion length due to elastic coupling in the liquid crystal has been neglected. The dynamics of the liquid crystals is much slower than the settling of the cavity field; thus, E_c adiabatically follows the evolution of n_0 and n_1. By taking the wave propagation equation with the cavity boundary conditions, the cavity field can be expressed as

$$E_c = i \sum_{k=0}^{\infty} [\hat{C} e^{in_0} J_0(2|n_1|)]^k \hat{C} e^{in_0} \frac{n_1}{|n_1|} J_1(2|n_1|) E_p, \tag{40}$$

where J_m is the Bessel function of the first kind and of order m, and $\hat{C}$ is an operator accounting for the geometry of the cavity and losses,

$$\hat{C} = \Gamma^{1/2} e^{i\delta} \hat{S}_x e^{i(L_0 \nabla_\perp^2/2k_p)} e^{-i(k_p \vec{r}_\perp^2/2f)} e^{i(L_1 \nabla_\perp^2/2k_p)},$$

with $1 - \Gamma$ the photon losses and δ the phase retardation in a round-trip. $\hat{S}_x$ is a symmetry operator that inverts the x axis, thus accounting for the odd number of mirrors, $\nabla_\perp^2$ is the transverse Laplacian and $\vec{r}_\perp$ the position in the transverse (x, y) plane.

In order to account for the finite size of the LCLV and the diaphragm inserted near the lens, a spatial filter with radius equal to 0.4 cm and a Fourier filter with radius $k = 6.4 \times 10^{-3}$ rad are used in the simulations. As for the other parameters, the liquid crystal response time is set to $\tau = 0.1$ s, the photon loss fraction $1 - \Gamma$ in between 0.7 and 0.8, and α is chosen in such a way that the unit is the pump threshold for the activation of the cavity field.

Starting with a random initial condition, a transient speckle-like behavior is observed, then a symmetry breaking occurs. The symmetry breaking becomes evident by plotting the numerical intensity $|E_c|^2$ in the z–y plane, as shown in Fig. 33a. The yellow line in $z = 0$ represents the position of the LCLV inside the cavity. As a consequence, there is an inhomogeneous build-up of the field, which induces large deviations from Gaussianity.

The numerical PDF of the cavity field intensity are displayed in Fig. 33b for different values of the pump. The intensities are rescaled in such a way that the PDF have the same slope at the origin. The tails are increasingly populated as the pump increases, in agreement with the experimental observations.

14.2.1. The hyper-cycle model

The nonlocal coupling between the cavity modes induces an inhomogeneous build-up of the field. Local domains of the cavity field are coupled with other, and distant, domains, thus introducing large loops of amplification, a mechanism similar to the hyper-cycle chain of reactions in the catalytic processes [14]. Because of this mechanism, there is a sort of focusing, for which at some space locations the cavity field grows much more with respect to the surrounding places, giving rise to large amplitude peaks and, thus, to large deviations from the Gaussian statistics.

To elucidate this mechanism, a simple two-mode model has been proposed, where only the evolution of the average refractive index n_1 is kept, the average being performed over the transverse plane. For a nearly plane cavity, $\bar{n}_1$ satisfies an equation of the form

$$\tau \frac{\partial \bar{n}_1}{\partial t} = -\bar{n}_1 + I_p F(\bar{n}_1), \tag{41}$$

where the first and second terms account for the liquid crystal relaxation and, respectively, the grating feeding provided by the pump and cavity fields. A cubic function is taken as an ansatz for F, which describes a linear growth followed by saturation, this last one being mainly due to multiple scattering processes [199].

When the nearly plane cavity is replaced by a cavity nearly spherical, the above mean-field picture is modified by the nonlocal coupling due to the inversion of the y-axis after a round trip. Therefore, two mean fields $\bar{n}_+$ and $\bar{n}_-$ must be considered, where the averages are performed over the upper and lower half-planes, respectively. Accounting for the inversion $y \to -y$ of the cavity field, the grating $\bar{n}_\pm$ is fed, after a round trip, by the grating $\bar{n}_\mp$ at the opposite side, i.e, the previous equation is replaced by the two following ones,

$$\begin{aligned} \tau \frac{\partial \bar{n}_+}{\partial t} &= -\bar{n}_+ + I_p F(\bar{n}_-), \\ \tau \frac{\partial \bar{n}_-}{\partial t} &= -\bar{n}_- + I_p F(\bar{n}_+), \end{aligned} \tag{42}$$

where it is implicitly assumed that the cavity losses are very high, i.e., the cavity field is negligible after more than one round trip.

The main features of F can be captured by the cubic function $F(\bar{n}_\pm) = \bar{n}_\pm - \bar{n}_\pm^3$. It is easy to show that for $1 < I_p < 2$, Eqs. (43) have only one stable solution, $\bar{n}_- = \bar{n}_+ = 0$, whereas for $I_p \geq 2$ a bifurcation occurs with the birth of the two stable asymmetric states

$$\begin{aligned} n_+ &= \frac{1}{\sqrt{2}} \sqrt{1 \pm \sqrt{\frac{I_p^2 - 4}{I_p^2}}}, \\ n_- &= \frac{1}{\sqrt{2}} \sqrt{1 \mp \sqrt{\frac{I_p^2 - 4}{I_p^2}}}, \end{aligned} \tag{43}$$

which breaks the $y \to -y$ symmetry, thus qualitatively accounting for the experimental and numerical observations.

As an indicator of the deviation from the exponential statistics a nondimensional parameter can be defined [15]

$$D(\vec{r}) = \frac{\langle I^2(\vec{r}) \rangle}{\langle I(\vec{r}) \rangle^2} - 2, \tag{44}$$

which is equal to zero for an exponential statistics and increases as c_1 decreases. Fig. 34 shows the numerically calculated $D(x)$, which is $D(\vec{r})$ integrated along the vertical axis, as a function of the horizontal transverse coordinate x and for $I_p/I_{th} = 4, 6, 8$. We see that $D(x)$ is an increasing function of both I_p and $|x|$. While for increasing I_p the nonlinearity increases, moving away from $x = 0$, (that is the inversion symmetry axis of the system), the inhomogeneity also increases because of the symmetry breaking introduced by the cavity configuration.

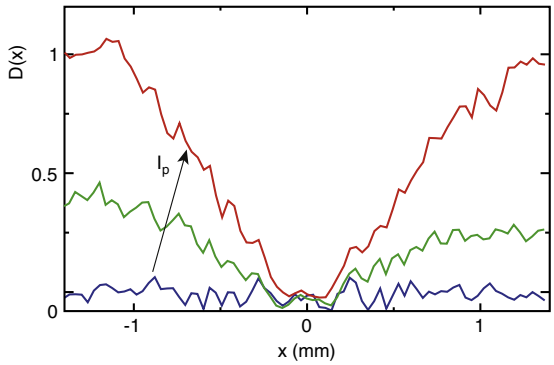

Fig. 34. Numerically calculated nondimensional indicator of rogue wave statistics for a nonlinear optical cavity vs the transverse coordinate x and for increasing pump intensity; $I_p/I_{th} = 4, 6, 8$ for the blue (lower), green (middle) and red (higher) curves.
Source: From Ref. [15].

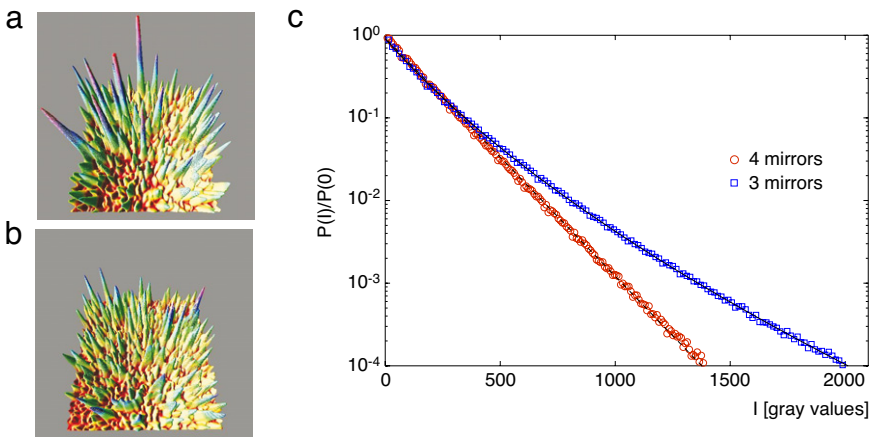

Fig. 35. Experimental intensity profiles for (a) the three-mirror cavity and (b) the four-mirror cavity. (c) Experimental PDF of the intensity for the four-mirror cavity (red circles) and the three-mirror cavity (blue squares). The four-mirror cavity distribution is practically exponential (dashed black line) while the three-mirror cavity is fitted by a stretched exponential (solid black line).
Source: From [200].

14.2.2. The role of inhomogeneity

The role of inhomogeneity in inducing a stretched exponential of the intensity has been experimentally investigated by building a cavity with four, instead of three, mirrors, thus, removing the spatial symmetry breaking. Indeed, for the four-mirror configuration there is no inversion symmetry. A direct comparison is made for the resulting PDF of the intensity with the case of a three-mirror cavity. In both cases the Fresnel number is fixed to $F = 125$ and the pump intensity to $I_p = 5$ mW/cm^2. The voltage applied to the LCLV is fixed to $V_0 = 40$ V r.m.s., $f = 30$ Hz, for the three-mirror cavity and to $V_0 = 32$ V r.m.s., $f = 30$ Hz, for the four-mirror cavity. These values are chose in such a way that for low pump intensity the PDF of the cavity field show the most similar exponential behavior.

For a qualitative comparison, in Fig. 35a and b are shown two intensity profiles obtained from two instantaneous images recorded for the three and four-mirror cavity, respectively. Rogue waves can be easily distinguished on the profiles recorded for the three-mirror cavity while they are not observed in the typical profiles recorded for the four-mirror cavity. Indeed, rogue waves appearance becomes much less probable in the absence of symmetry breaking.

The PDF of the intensity are recorded in a similar way as described above, both for the three and the four-mirror cavity. The results are plotted in Fig. 35c. As it can be appreciated from the fitting curves, while for the three-mirror cavity the behavior is well described by a stretched exponential, for the four-mirror cavity the data are quite well fitted by an exponential function. A Gaussian field statistics is, therefore, recovered when removing the inhomogeneity brought forth by the cavity configuration.

14.3. Rogue waves in a linear optical experiment

In order to outline the two key ingredients for the appearance of optical rogue waves, namely, granularity and inhomogeneity, a linear optical experiment has been setup. Here, granularity, that is, fragmentation of the wave field into

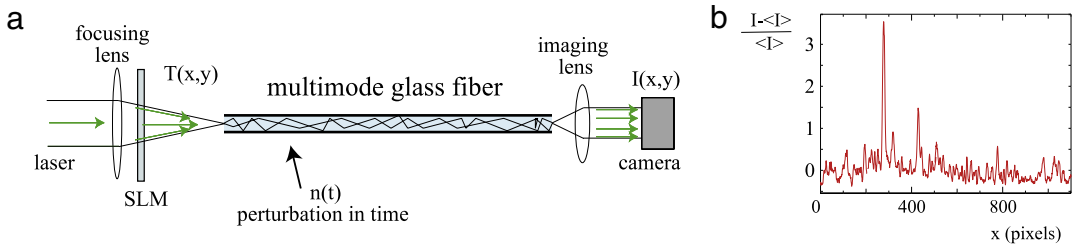

Fig. 36. (a) Experimental setup for the linear excitation of optical rogue waves: a laser input beam is focused into a multimode glass fiber; the output field is imaged onto a CCD camera; a SLM controls the input beam profile through variable transmittance masks $T(x, y)$; a lateral perturbation $n(t)$ rules the fiber bending; (b) 1D intensity profile $I(x)$ taken from a corresponding image; $\langle I \rangle$ is the intensity averaged over the whole image.
Source: From Ref. [15].

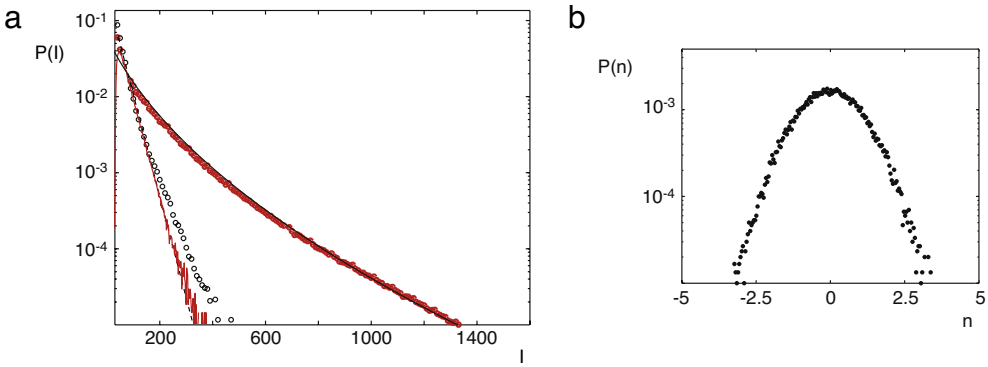

Fig. 37. (a) PDF of the intensity at the output of the fiber; solid (red) line: homogeneous mask; (black) empty dots: inhomogeneous mask; (red) filled dots: inhomogeneous mask and temporal perturbations; the black dashed line is a fit with an exponential function; the black solid line is a fit with a stretched exponential fit ($c_1 = 10$, $c_2 = 0.092$). (b) Gaussian PDF of the perturbation $n(t)$ used to drive the fiber and producing the large-tailed PDF. (For interpretation of the references to colour in this figure legend, the reader is referred to the web version of this article.)
Source: From Ref. [15].

a large number of elementary objects of still finite size, let us call them speckles, and inhomogeneity, that is, clustering of speckles in spatial domains with different average intensities, can be separately controlled.

A schematic representation of the experimental setup is shown in Fig. 36a. It consists of a multi-mode glass optical fiber (0.4 mm diameter and 2 m length) in which a laser beam is let to propagate. The input beam comes from a frequency doubled solid state laser, wavelength 532 nm. Less than 1 mW/cm^2 is coupled inside the fiber and the input profile is controlled by a spatial-light-modulator, SLM. This is a computer driven liquid crystal display, 768 $\times$ 1024 pixels, one inch diagonal size. By setting onto the SLM appropriate transmittance masks $T(x, y)$, arbitrary profiles of the input intensity distribution can be introduced.

While an uniform mask $T(x, y)$ allows the whole cone of input wave vectors to be coupled into the fiber, an inhomogeneous mask with a black hole prevents the wave vectors passing in that direction to be coupled into the fiber, thus inducing at the output domains of different average intensity. This symmetry breaking mechanism introduce high amplitude peaks on the output intensity distributions $I(x, y)$. In Fig. 36b a one-dimensional intensity profiles taken along an x-line of a corresponding image is displayed for the inhomogeneous case. A large amplitude peak, or optical rogue wave, can be clearly distinguished.

The average size of the grains (single speckle) is given by the effective aperture of the fiber, the total number of modes supported by the fiber being proportional to $(a/\lambda)2$, with a the radius of the fiber core and λ the wavelength of light in air [201]. For the typical experimental conditions, the total number of modes can be estimated as $\sim 10^6$. On the other hand, the inhomogeneous mask induces at the exit of the fiber an inhomogeneous distribution of the average intensity when it is evaluated over domains of adjacent grains. By acquiring with a CCD camera (768 $\times$ 1024 pixels and 16 bits depth) a large set of images (about one thousand) and then performing the histograms of the intensity values on the whole image stack, the PDFs of the intensity are determined.

The results are shown in Fig. 37a, where the PDF recorded for a uniform $T(x, y)$ is compared with the PDF recorded in the presence of an inhomogeneous mask. The first one (red solid line) is well fitted by an exponential function (black dashed line), as expected for speckles [201]. The second one (empty black dots) shows appreciable, though not too large, deviations from the exponential. In the same figure, a PDF with strong deviations from the exponential is also plotted; it is obtained by applying to the fiber a lateral perturbation $n(t)$ with a Gaussian distribution of the amplitude, as displayed in Fig. 37b. The perturbation is realized by placing a piezoelectric emitter in contact with a side of the fiber (see Fig. 36a).

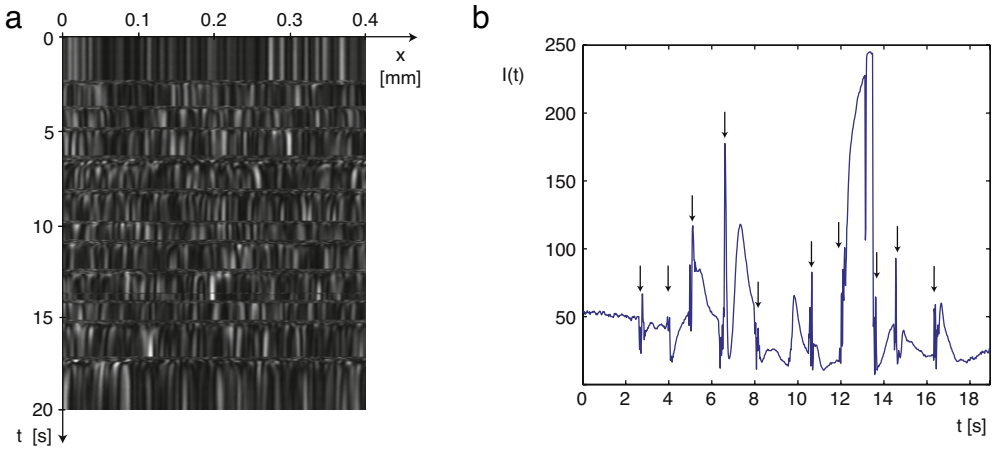

Fig. 38. (a) Spatiotemporal plots showing the evolution of the intensity when pulse-like perturbations $n(t)$ are applied to the fiber. (b) Corresponding spatially averaged intensity as a function of time; arrows indicate the instant times when the $n(t)$ impulses are released.

Thanks to the elasto-optical effect, when the piezo emits a low frequency acoustic wave, it locally modifies the optical paths inside the fiber, giving rise to a different spatial distribution of the output intensity, therefore, the detector collects events over different speckle configurations. Note that in the nonlinear experiment the multimode dynamics spontaneously introduces a continuous change of the cavity field, hence, allowing to explore a large number of configurations.

The effect of the temporal modulation greatly enhances the stretched exponential character of the PDF of the intensity. Note, however, that in the inhomogeneous case the PDF is a stretched exponential even without temporal perturbations (even though small-tailed when compared to the perturbed case), while in the homogeneous case the PDF remains exponential even in the presence of temporal modulations.

When inhomogeneity and temporal perturbations are simultaneously present, the resulting large-tailed PDF of the intensity is well described by a stretched exponential distribution, that is, $P(I) = e^{-\sqrt{c_1+c_2 I}}$, where c_2 is a scale factor and c_1 a form parameter. In the limit $c_1 \to \infty$, the stretched distribution becomes an exponential. To account for the stretched exponential character of the PDF let us consider the role of inhomogeneity. At the fiber exit the intensity is distributed as a collection of speckle patterns made of various domains with different average intensity. Within a single domain the statistics is exponential but the variance changes from domain to domain. As a consequence, the overall PDF becomes a stretched exponential as the events are counted over the whole field. More precisely, the stretched distribution can be obtained as a statistical mixture of many exponential distributions with different variance,

$$P(I) = \int_0^\infty d\sigma\, \rho(\sigma) \frac{e^{-I/\sigma}}{\sigma}, \tag{45}$$

where σ is the variance of the PDF in a single domain. The stretched distribution is exactly obtained when the distribution of σ is

$$\rho(\sigma) = \sqrt{\sigma}\, e^{-\frac{c_2\sigma}{4} - \frac{c_1}{c_2\sigma}}. \tag{46}$$

Qualitatively, this prediction is well confirmed by the experimental results, where $\rho(\sigma)$ has been evaluated by performing the PDF analysis over small spatial domains and determining the local variance σ of the associated fit [15].

14.4. Log-Poisson statistics of the return times

The statistics of the waiting times between successive rogue waves occurring at a given space position have been considered in the optical fiber experiment. By limiting the observations to a single homogeneous domain, it is possible to classify a Poisson distribution of event separation. However, as $n(t)$ jumbles the different domains within the detector aperture, different rates associated with different domains are expected. Interpolation of the different Poissonian should yield a log-Poisson statistics for the waiting times between two successive events [202,203].

In the experiment, the fiber is driven by the piezoelectric perturbation $n(t)$, by sending an impulse and, then, letting the dynamics to relax. A typical spatio-temporal plot is shown in Fig. 38a, where, after each impulse, a new configuration, followed by a slowing-down readjustment, is observed. In Fig. 38b the spatially averaged intensity is plotted as a function of time, with arrows indicating the instant times when the $n(t)$ impulse is released.

The waiting time between successive events is defined as $w = \ln(t_k) - \ln(t_{k-1}) = \ln(t_k/t_{k-1})$, where t_k is the occurrence time of the k-th event. To obtain the PDF of the waiting times, the events are recorded by placing a photodiode in a fixed point and then counting a rogue wave each time the intensity is above a given threshold, here taken as four times the average

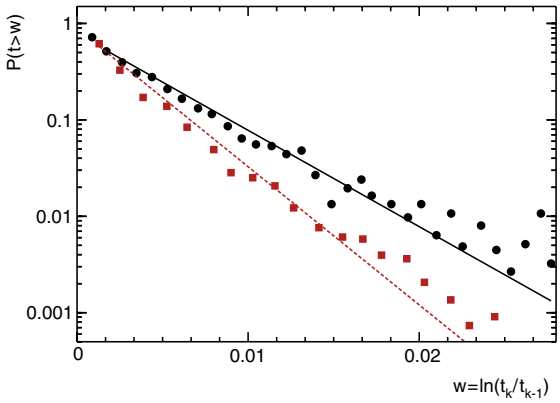

Fig. 39. Log-Poisson distribution of the waiting times between successive rogue waves; (red) squares, (black) dots, correspond to low, respectively, high amplitudes of $n(t)$.
Source: From Ref. [15].

intensity. The analysis of the recorded data over a large number of configurations, each one triggered by the application of a $n(t)$ impulse, yields a log-Poisson distribution of the waiting time between successive rogue waves, as depicted in Fig. 39.

15. Conclusions

Rogue waves are ubiquitous phenomena that were first brought into evidence by the oceanographers, since the appearance of monster waves on the ocean surfaces has become beyond the legend of mariner tales and has been confirmed as being at the origin of real, extremely dangerous, events. Then, rogue waves have been observed in such different physical contexts as superfluid Helium, nonlinear optics, capillary waves, plasma waves and Bose–Einsteins condensates. Often, the common nature of these different systems can be searched in their universal description, which is based on the nonlinear Schrödinger equation. In this case, rogue waves are understood as the results of modulational instability and the subsequent formation of oscillating envelope solitons. Rogue waves can be explained also in terms of inverse cascade and in some systems they arise even in the absence of nonlinearity. The question remains open how to link all the different systems under a common description, able to account for the different mechanisms generating the rogue waves.

Moreover, there is not yet a common definition of rogue waves. Each system displays his specificity and, especially, the statistical behavior is not described by an universal distribution, even though a common feature of all rogue wave phenomena is the occurrence of significant deviations from the Gaussianity. Another problem is the ambiguity sometimes arising from the classification of extreme events as rogue waves, the two not necessarily coinciding. Indeed, rogue waves require the existence of a dispersion relation and of a coherent build-up of large amplitude pulses through the collision/interference of solitons/wavepackets traveling with different group velocities.

The aim of the presented review was not to be exhaustive of all the rogue wave phenomena reported in the literature, neither to provide a common explanation, but of guiding the reader through a gallery of representative examples, where the main physical mechanisms at the origin of rogue waves are elucidated and, when possible, compared. For instance, from the large part of the results presented, it emerges that nonlinearity and nonlocal coupling are mechanisms that play a key role in originating rogue waves. In this context, linear experiments, either in optics or in microwaves, have the role of highlighting the essential role of granularity, that is, the fragmentation of the field in fundamental grains of activity, such as solitons arising from the modulational instability or dispersive wavepackets in the linear case. Once grains activated, the spatial inhomogeneity acts as a nonlocal coupling that provides a coherent build-up of rogue waves in different space/time positions.

It must be stressed that in all the considered systems rogue waves are the result of the dispersive properties of ensembles of many waves. In these systems, the nonlinearity needs not necessarily to be strong, provided the spatial inhomogeneity plays its role of mixing-up the individual grains of activity.

Acknowledgments

D. Proment is acknowledged for discussions. M.O. was supported by EU, project EXTREME SEAS (SCP8-GA-2009-234175) and ONR grant N000141010991. M.O. acknowledges Dr. GiuliNico for interesting discussions. Research at Perimeter Institute for Theoretical Physics is supported in part by the Government of Canada through NSERC and by the Province of Ontario through MRI. S.R and U.B. acknowledge the ANR international program, project ANR-2010-INTB-402-02, "COLORS".

References

[1] P. Müller, C. Garrett, A. Osborne, Rogue waves – the fourteenth 'Aha Huliko' a Hawaiian winter workshop, Oceanography 18 (3) (2005) 66–75.
[2] B. White, On the chance of freak waves at sea, Journal of Fluid Mechanics 355 (1998) 113–138.
[3] N. Akhmediev, E. Pelinovsky, Discussion & debate: Rogue waves – towards a unifying concept? European Physical Journal - Special Topics 185 (1) (2010) 1–266.
[4] M. Onorato, A. Osborne, M. Serio, S. Bertone, Freak wave in random oceanic sea states, Physical Review Letters 86 (25) (2001) 5831–5834.
[5] J.S.-C.N. Akhmediev, A. Ankiewicz, Extreme waves that appear from nowhere: on the nature of rogue waves, Physics Letters A 373 (25) (2009) 2137–2145.
[6] A. Dyachenko, V. Zakharov, On the formation of freak waves on the surface of deep water, JETP Letters 88 (5) (2008) 307–311.
[7] K. Hammani, B. Kibler, C. Finot, A. Picozzi, Emergence of rogue waves from optical turbulence, Physics Letters A 374 (34) (2010) 3585–3589.
[8] M. Onorato, T. Waseda, A. Toffoli, L. Cavaleri, O. Gramdstad, P.A.E.M. Janssen, K.T. , J. Monbaliu, N. Mori, A.R. Osborne, M. Serio, C. Stansberg, H. Tamura, K. Trulsen, Statistical properties of directional ocean waves: the role of the modulational instability in the formation of extreme events, Physical Review Letters 102 (2009) 114502(4).
[9] D. Solli, C. Ropers, P. Koonath, B. Jalali, Optical rogue waves, Nature 450 (7172) (2007) 1054–1057.
[10] J.M. Dudley, G. Genty, B.J. Eggleton, Harnessing and control of optical rogue waves in supercontinuum generation, Optics Express 16 (6) (2008) 3644–3651.
[11] A. Ganshin, V. Efimov, G. Kolmakov, L. Mezhov-Deglin, P. Mcclintock, Observation of an inverse energy cascade in developed acoustic turbulence in superfluid Helium, Physical Review Letters 101 (6) (2008) 1–4.
[12] A. Montina, U. Bortolozzo, S. Residori, F.T. Arecchi, Non-Gaussian statistics and extreme waves in a nonlinear optical cavity, Physical Review Letters 103 (17) (2009) 173901.
[13] R. Höhmann, U. Kuhl, H.-J. Stöckmann, L. Kaplan, E.J. Heller, Freak waves in the linear regime: a microwave study, Physical Review Letters 104 (9) (2010) 1–4.
[14] M. Eigen, P. Schuster, The Hypercycle: A Principle of Natural Self-Organization, Springer, Berlin, 1979.
[15] F.T. Arecchi, U. Bortolozzo, A. Montina, S. Residori, Granularity and inhomogeneity are the joint generators of optical rogue waves, Physical Review Letters 106 (15) (2011) 153901.
[16] G. Clauss, Dramas of the sea: episodic waves and their impact on offshore structures, Applied Ocean Research 24 (3) (2002) 147–161.
[17] M. Brown, A. Jensen, Experiments on focusing unidirectional water waves, Journal of Geophysical Research 106 (C8) (2001) pp. 16 917–16.
[18] T. Baldock, C. Swan, P. Taylor, A laboratory study of nonlinear surface waves on water, Philosophical Transactions of the Royal Society of London. Series A: Mathematical, Physical and Engineering Sciences 354 (1707) (1996) 649–676.
[19] T. Johannessen, C. Swan, A laboratory study of the focusing of transient and directionally spread surface water waves, Proceedings of the Royal Society of London. Series A: Mathematical, Physical and Engineering Sciences 457 (2008) (2001) 971–1006.
[20] C. Fochesato, S. Grilli, F. Dias, Numerical modeling of extreme rogue waves generated by directional energy focusing, Wave Motion 44 (5) (2007) 395–416.
[21] B. Kinsman, Wind Waves, Prentice-Hall, 1965.
[22] P.A.E.M. Janssen, The Interaction of Ocean Waves and Wind, Cambridge University Press, Cambridge, 2004.
[23] C. Kharif, E. Pelinovsky, A. Slunyaev, Rogue Waves in the Ocean, Springer Verlag, 2009.
[24] G. Komen, L. Cavaleri, M. Donelan, K. Hasselmann, H. Hasselmann, P. Janssen, Dynamics and Modeling of Ocean Waves, Cambridge University Press, Cambridge, 1994.
[25] K. Hasselmann, T. Barnett, E. Bouws, H. Carlson, D. Cartwright, K. Enke, J. Ewing, H. Gienapp, D. Hasselmann, P. Kruseman, et al., Measurements of wind-wave growth and swell decay during the joint North Sea wave project (jonswap), Ergnzungsheft zur Deutschen Hydrographischen Zeitschrift Reihe 8 (12) (1973).
[26] D. Hauser, K. Kahma, H. Krogstad, J. Monbaliu, S. Lehner, L. Wyatt, (Eds.) Measuring and Analysing the directional spectrum of ocean waves, ser. COST 714; EUR 21367. COST Office, 2005.
[27] M. Onorato, L. Cavaleri, S. Fouques, O. Gramstad, P.A.E.M. Janssen, J. Monbaliu, A.R. Osborne, C. Pakozdi, M. Serio, C. Stansberg, A. Toffoli, K. Trulsen, Statistical properties of mechanically generated surface gravity waves: a laboratory experiment in a 3d wave basin, Journal of Fluid Mechanics 627 (2009) 235–257.
[28] W. Munk, Proposed uniform procedure for observing waves and interpreting instrument records, SIO Wave Project. Translations by DD Bidde and RL Wiegel can be found in Translations of Four French, 1944.
[29] M.A. Tayfun, Narrow-band nonlinear sea waves, Journal of Geophysical Research 85 (C3) (1980) 1548–1552.
[30] I. Nikolkina, I. Didenkulova, Catalogue of rogue waves reported in media in 2006–2010, Natural Hazards (2011) 1–18.
[31] S. Haver, Evidences of the existence of freak waves, in: Rogue Waves 2000: Proceedings of a Workshop Organized by Ifremer and Held in Brest, France, 29–30 November 2000, within de Brest SeaTechWeek 2000, 32. Editions Quae, 2001, 129.
[32] E. Bitner-Gregersen, A. Magnusson, Extreme events in field data and in a second order wave model, in: Rogue Waves, 2004.
[33] C. Guedes soares, Z. Cherneva, E. Antão, Characteristics of abnormal waves in North Sea storm sea states, Applied Ocean Research 25 (6) (2003) 337–344.
[34] U. De pinho, P. Liu, C. Ribeiro, Freak waves at campos basin, Brazil, Geofizika 21 (2004).
[35] N. Mori, P. Liu, T. Yasuda, Analysis of freak wave measurements in the Sea of Japan, Ocean Engineering 29 (11) (2002) 1399–1414.
[36] H. Tomita, T. Kawamura, Statistical analysis and inference from the in-situ data of the Sea of Japan with reference to abnormal and/or freak waves, in: Proceedings of the International Offshore and Polar Engineering Conference, Seattle, WA, USA, vol. 3, 2000, pp. 116–122.
[37] J. Schulz-Stellenfleth, S. Lehner, Measurement of 2-d sea surface elevation fields using complex synthetic aperture radar data, Geoscience and Remote Sensing, IEEE Transactions on 42 (6) (2004) 1149–1160.
[38] J. Nieto borge, S. Lehner, A. Niedermeier, J. Schulz-Stellenfleth, Detection of ocean wave groupiness from spaceborne synthetic aperture radar, Journal of Geophysical Research 109 (2004).
[39] P. Janssen, W. Alpers, Why sar wave mode data of ers and envisat are inadequate for giving the probability of occurrence of freak waves, in: Proceedings of the SEASAR 2006 Workshop, ESA/ESRIN, 2006.
[40] L. Wyatt, J. Green, Measuring high and low waves with hf radar, in: OCEANS 2009-EUROPE, IEEE, 2009, pp. 1–5.
[41] P.A.E.M. Janssen, Nonlinear four-wave interaction and freak waves, Journal of Physical Oceanography 33 (4) (2003) 863–884.
[42] A. Toffoli, A. Babanin, M. Onorato, T. Waseda, Maximum steepness of oceanic waves: field and laboratory experiments, Geophysical Research Letters 37 (5) (2010) L05603.
[43] P. Janssen, On some consequences of the canonical transformation in the Hamiltonian theory of water waves, Journal of Fluid Mechanics 637 (1) (2009) 1–44.
[44] A. Osborne, M. Onorato, M. Serio, Nonlinear fourier analysis of deep-water, random surface waves: Theoretical formulation and experimental observations of rogue waves, in: Proc 14th Aha Huliko a Winter Workshop, Honolulu, Hawaii, 2005.
[45] A. Osborne, Nonlinear Ocean Waves, Academic Press, 2010.
[46] A. Islas, C. Schober, Predicting rogue waves in random oceanic sea states, Physics of Fluids 17 (2005) 031701.
[47] A. Slunyaev, Nonlinear analysis and simulations of measured freak wave time series, European Journal of Mechanics-B/Fluids 25 (5) (2006) 621–635.
[48] T.B. Benjamin, J.E. Feir, The disintegration of wave trains on deep water. Part I. Theory, Journal of Fluid Mechanics 27 (1967) 417–430.
[49] V. Zakharov, Stability of period waves of finite amplitude on surface of a deep fluid, Journal of Applied Mechanics and Technical Physics 9 (1968) 190–194.

[50] V. Zakharov, L. Ostrovsky, Modulation instability: the beginning, Physica D: Nonlinear Phenomena 238 (5) (2009) 540–548.
[51] N. Akhmediev, V. Eleonskii, N. Kulagin, Exact first-order solutions of the nonlinear Schrödinger equation, Theoretical and Mathematical Physics 72 (2) (1987) 809–818.
[52] E. Kuznetsov, Solitons in a parametrically unstable plasma, in: Akademiia Nauk SSSR Doklady, 236, 1977, pp. 575–577.
[53] K.B. Dysthe, K. Trulsen, Note on breather type solutions of the NLS as models for freak-waves, Physica Scripta T82 (1999) 48–52.
[54] A. Osborne, M. Onorato, M. Serio, The nonlinear dynamics of rogue waves and holes in deep-water gravity wave train, Physics Letters A 275 (2000) 386–393.
[55] A. Galchenko, A. Babanin, D. Chalikov, I. Young, T. Hsu, Modulational instabilities and breaking strength for deep-water wave groups, Journal of Physical Oceanography (2010).
[56] D. Peregrine, Water waves, nonlinear Schrödinger equations and their solutions, Journal of the Australian Mathematical Society Series 25 (1) (1983) 16–43.
[57] N. Akhmediev, A. Ankiewicz, M. Taki, Waves that appear from nowhere and disappear without a trace, Physics Letters A 373 (6) (2009) 675–678.
[58] V. Shrira, V. Geogjaev, What makes the Peregrine soliton so special as a prototype of freak waves? Journal of Engineering Mathematics 67 (1) (2010) 11–22.
[59] A. Chabchoub, N. Hoffmann, N. Akhmediev, Rogue wave observation in a water wave tank, Physical Review Letters 106 (20) (2011) 204502.
[60] B. Kibler, J. Fatome, C. Finot, G. Millot, F. Dias, G. Genty, N. Akhmediev, J. Dudley, The Peregrine soliton in nonlinear fibre optics, Nature Physics 6 (10) (2010) 790–795.
[61] H. Bailung, S.K. Sharma, Y. Nakamura, Observation of Peregrine solitons in a multicomponent plasma with negative ions, Physical Review Letters 107 (2011) 255005.
[62] A. Chabchoub, S. Neumann, N. Hoffmann, N. Akhmediev, Spectral properties of the Peregrine soliton observed in a water wave tank, Journal of Geophysical Research 117 (2012) C00J03.
[63] N. Akhmediev, A. Ankiewicz, J. Soto-Crespo, J. Dudley, Rogue wave early warning through spectral measurements? Physics Letters A (2010).
[64] N. Akhmediev, J. Soto-Crespo, A. Ankiewicz, N. Devine, Early detection of rogue waves in a chaotic wave field, Physics Letters A (2011).
[65] N. Akhmediev, V. Eleonskii, N. Kulagin, Generation of periodic trains of picosecond pulses in an optical fiber: exact solutions, Soviet Physics JETP 62 (5) (1985) 894–899.
[66] N. Akhmediev, V. Korneev, Modulation instability and periodic solutions of the nonlinear Schrödinger equation, Theoretical and Mathematical Physics 69 (2) (1986) 1089–1093.
[67] Y. Ma, The perturbed plane-wave solutions of the cubic Schrödinger equation, Studies in Applied Mathematics 60 (1979) 43–58.
[68] N. Karjanto, Mathematical aspects of extreme water waves, 2006.
[69] N. Akhmediev, A. Ankiewicz, J. Soto-Crespo, Rogue waves and rational solutions of the nonlinear Schrödinger equation, Physical Review E 80 (2) (2009) 026601.
[70] N. Akhmediev, A. Ankiewicz, Solitons: Nonlinear Pulses and Beams, Chapman & Hall London, 1997.
[71] A. Calini, C. Schober, Homoclinic chaos increases the likelihood of rogue wave formation, Physics Letters A 298 (5–6) (2002) 335–349.
[72] M. Ablowitz, B. Herbst, On homoclinic structure and numerically induced chaos for the nonlinear Schrodinger equation, SIAM Journal on Applied Mathematics (1990) 339–351.
[73] A. Chabchoub, N. Hoffmann, M. Onorato, A. Akhmediev, Super rogue waves: observation of a higher order breather in water waves, Physical Review X 2 (1) (2011) 011015.
[74] H. Yuen, B. Lake, Nonlinear dynamics of deep-water gravity waves, Advances in Applied Mechanics 22 (67) (1982) 229.
[75] M.P. Tulin, T. Waseda, Laboratory observation of wave group evolution, including breaking effects, Journal of Fluid Mechanics 378 (1999) 197–232.
[76] N. Karjanto, E. Van groesen, Qualitative comparisons of experimental results on deterministic freak wave generation based on modulational instability, Journal of Hydro-Environment Research 3 (4) (2010) 186–192.
[77] G. Clauss, M. Klein, M. Onorato, Formation of extraordinarily high waves in space and time, in: Proceedings of the ASME 2011 30th International Conference on Ocean, Offshore and Arctic Engineering, June 19–24, 2011, Rotterdam, The Netherlands, 2011, pp. 1–13.
[78] B. Kibler, J. Fatome, C. Finot, G. Millot, G. Genty, B. Wetzel, N. Akhmediev, F. Dias, J. Dudley, Observation of Kuznetsov–Ma soliton dynamics in optical fibre, Scientific Reports 2 (2012).
[79] I. Ten, H. Tomita, Simulation of the ocean waves and appearance of freak waves, in: Reports of RIAM Symposium No. 17SP1-2, Proceedings of a symposium held at Chikushi Campus, Kyushu University, Kasuga, Fukuoka, Japan, 10–11 March, 2006, pp. 1–14.
[80] H. Hasimoto, H. Ono, Nonlinear modulation of gravity waves, Journal of Physical Society of Japan 33 (3) (1972) 805–811.
[81] P.A.E.M. Janssen, M. Onorato, The intermediate water depth limit of the Zakharov equation and consequences for wave prediction, Journal of Physical Oceanography 37 (2007) 2389–2400.
[82] M. Francius, C. Kharif, Three-dimensional instabilities of periodic gravity waves in shallow water, Journal of Fluid Mechanics 561 (2006) 417–438.
[83] K. Henderson, D. Peregrine, J. Dold, Unsteady water wave modulations: fully nonlinear solutions and comparison with the nonlinear Schrödinger equation, Wave Motion 29 (4) (1999) 341–361.
[84] K.B. Dysthe, Note on the modification of the nonlinear Schrödinger equation for application to deep water waves, Proceedings of The Royal Society of London. Series A A 369 (1979) 105–114.
[85] O. Gramstad, K. Trulsen, Hamiltonian form of the modified nonlinear Schrödinger equation for gravity waves on arbitrary depth, Journal of Fluid Mechanics 670 (2011) 404–426.
[86] D. Clamond, M. Francius, J. Grue, C. Kharif, Long time interaction of envelope solitons and freak wave formations, European Journal of Mechanics-B/Fluids 25 (2006) 536–553.
[87] V. Zakharov, A. Dyachenko, A. Prokofiev, Freak waves as nonlinear stage of Stokes wave modulation instability, European Journal of Mechanics/B Fluids 25 (5) (2006) 677–692.
[88] M. Onorato, A.R. Osborne, M. Serio, C. Brandini, C.T. Stansberg, Observation of strongly non-Gaussian statistics for random sea surface gravity waves in wave flume experiments, Physical Review E 70 (2004) 067302.
[89] M. Onorato, A. Osborne, M. Serio, L. Cavaleri, Modulational instability and non-Gaussian statistics in experimental random water-wave trains, Physics of Fluids 17 (2005) 078101.
[90] M. Onorato, A. Osborne, M. Serio, L. Cavaleri, C. Brandini, C. Stansberg, Extreme waves modulational instability and second order theory: wave flume experiments on irregular waves, European Journal of Mechanics-B/Fluids 25 (2006) 586–601.
[91] F. Fedele, Z. Cherneva, M. Tayfun, C. Soares, Nonlinear Schrödinger invariants and wave statistics, Physics of Fluids 22 (2010) 036601.
[92] L. Shemer, A. Sergeeva, A. Slunyaev, Effect of the initial spectrum on the spatial evolution of statistics of unidirectional nonlinear random waves, Physics of Fluids 22 (2010) 016601.
[93] M. Tayfun, J.-M. Lo, Non-linear effects on wave envelope and phase, Journal of Waterway, Port, Coastal, and Ocean Engineering (ASCE) 116 (1992) 79–100.
[94] N. Mori, Occurrence probability of a freak wave in a nonlinear wave field, Ocean Engineering 31 (2) (2004) 165–175.
[95] N. Mori, P.A.E.M. Janssen, On kurtosis and occurrence probability of freak waves, Journal of Physical Oceanography 36 (2006) 1471–1483.
[96] N. Mori, M. Onorato, P.A.E.M. Janssen, A.R. Osborne, M. Serio, On the extreme statistics of long-crested deep water waves: theory and experiments, Journal of Geophysical Research 112 (C09011) (2007) http://dx.doi.org/10.1029/2006JC004024.
[97] Z. Cherneva, M. Tayfun, C. Soares, Statistics of nonlinear waves generated in an offshore wave basin, Journal of Geophysical Research 114 (C8) (2009) C08005.
[98] A. Slunyaev, Freak wave events and the wave phase coherence, The European Physical Journal-Special Topics 185 (1) (2010) 67–80.
[99] C. Brandini, Nonlinear interaction processes in extreme wave dynamics, Ph.D. Thesis, Universitá Di Firenze, 2001.

[100] N. Mori, T. Yasuda, Effects of high-order nonlinear interactions on unidirectional wave trains, Ocean Engineering 29 (2002) 1233–1245.
[101] D.G. Dommermuth, D.K. Yue, A high-order spectral method for the study of nonlinear gravity waves, Journal of Fluid Mechanics 184 (1987) 267–288.
[102] B.J. West, K.A. Brueckner, R.S. Jand, D.M. Milder, R.L. Milton, A new method for surface hydrodynamics, Journal of Geophysical Research 92 (C11) (1987) 11 803–11 824.
[103] P. Janssen, J. Bidlot, On the extension of the freak wave warning system and its verification, Technical Memorandum 588 (2009).
[104] A. Toffoli, M. Benoit, M. Onorato, E.M. Bitner-Gregersen, The effect of third-order nonlinearity on statistical properties of ransom directional waves in finite depth, Nonlinear Processes in Geophysics 16 (2009) 131–139.
[105] E. Pelinovsky, et al., Numerical modeling of the kdv random wave field, European Journal of Mechanics-B/Fluids 25 (4) (2006) 425–434.
[106] N. Mori, M. Onorato, P. Janssen, On the estimation of the kurtosis in directional sea states for freak wave forecasting, Journal of Physical Oceanography 41 (2011) 1484–1497.
[107] T. Waseda, T. Kinoshita, H. Tamura, Evolution of a random directional wave and freak wave occurrence, Journal of Physical Oceanography 39 (3) (2009) 621–639.
[108] M. Onorato, A.R. Osborne, M. Serio, On deviations from Gaussian statistics for surface gravity waves, in: Rogue Waves, Proceedings Hawaiian Winter Workshop, University of Hawaii at Manoa, USA, 2005.
[109] S. Annenkov, V. Shrira, Evolution of kurtosis for wind waves, Geophysical Research Letters 36 (L13603) (2009) L13603.
[110] T. Vinje, The statistical distribution of wave heights in a random seaway, Applied Ocean Research 11 (3) (1989) 143–152.
[111] M. Longuet-Higgins, The effect of non-linearities on statistical distribution in the theory of sea waves, Journal of Fluid Mechanics 17 (1963) 459–480.
[112] N. Sharma, R. Dean, Second-order directional seas and associated wave forces, Society of Petroleum Engineers Journal 4 (1981) 129–140.
[113] G. Forristall, Wave crests distributions: observations and second-order theory, Journal of Physical Oceanography 30 (2000) 1931–1943.
[114] M. Prevosto, H. Krogstad, A. Robin, Probability distributions for maximum wave and crest heights, Coastal Engineering 40 (2000) 329–360.
[115] A. Toffoli, M. Onorato, J. Monbaliu, Wave statistics in unimodal and bimodal seas from a second-order model, European Journal of Mechanics-B/Fluids 25 (5) (2006) 649–661.
[116] A. Toffoli, M. Onorato, A.V. Babanin, E. Bitner-Gregersen, A.R. Osborne, J. Monbaliu, Second-order theory and set-up in surface gravity waves: a comparison with experimental data, Journal of Physical Oceanography 37 (2007) 2726–2739.
[117] M.S. Longuet-Higgins, R.W. Stewart, Radiation stress and mass transport in surface gravity waves with application to "surf beats", Journal of Fluid Mechanics 13 (1962) 481–504.
[118] T. Adcock, P. Taylor, S. Yan, Q. Ma, P. Janssen, Did the Draupner wave occur in a crossing sea? Proceedings of the Royal Society A: Mathematical, Physical and Engineering Science 467 (2134) (2011) 3004–3021.
[119] C. Stansberg, Effects from directionality & spectral bandwidth on non-linear spatial modulations of deep-water surface gravity wave trains, in: Coastal Engineering Conference, 1. ASCE American Society of Civil Engineers, 1995, pp. 579–579.
[120] M. Onorato, A.R. Osborne, M. Serio, Extreme wave events in directional random oceanic sea states, Physics of Fluids 14 (4) (2002) 25–28.
[121] H. Socquet-Juglard, K. Dysthe, K. Trulsen, H. Krogstad, J. Liu, Distribution of surface gravity waves during spectral changes, Journal of Fluid Mechanics 542 (2005) 195–216.
[122] O. Gramstad, K. Trulsen, Influence of crest and group length on the occurrence of freak waves, Journal of Fluid Mechanics 582 (2007) 463–472.
[123] T. Waseda, T. Kinoshita, H. Tamura, Evolution of a random directional wave and freak wave occurrence, Journal of Physical Oceanography 39 (2009) 621–639.
[124] M. Onorato, L. Cavaleri, S. Fouques, O. Gramstad, P. Janssen, J. Monbaliu, A. Osborne, C. Pakozdi, M. Serio, C. Stansberg, et al., Statistical properties of mechanically generated surface gravity waves: a laboratory experiment in a three-dimensional wave basin, Journal of Fluid Mechanics 627 (2009) 235–257.
[125] A. Toffoli, O. Gramstad, K. Trulsen, J. Monbaliu, E. Bitner-Gregersen, M. Onorato, Evolution of weakly nonlinear random directional waves: laboratory experiments and numerical simulations, Journal of Fluid Mechanics 664 (1) (2010) 313–336.
[126] K. Trulsen, K.B. Dysthe, A modified nonlinear Schrödinger equation for broader bandwidth gravity waves on deep water, Wave Motion 24 (1996) 281–289.
[127] M. Tanaka, A method of studying nonlinear random field of surface gravity waves by direct numerical simulations, Fluid Dynamics Research 28 (2001) 41–60.
[128] T. Waseda, M. Hallerstig, K. Ozaki, H. Tomita, Enhanced freak wave occurrence with narrow directional spectrum in the North Sea, Geophysical Research Letters 38 (13) (2011) L13605.
[129] V. Ruban, Nonlinear stage of the Benjamin–Feir instability: three-dimensional coherent structures and rogue waves, Physical Review Letters 99 (4) (2007) 44502.
[130] V. Ruban, Quasiplanar steep water waves, Physical Review E 71 (5) (2005) 055303.
[131] V. Ruban, J. Dreher, Numerical modeling of quasiplanar giant water waves, Physical Review E 72 (6) (2005) 066303.
[132] V. Ruban, "Breathing" rogue wave observed in numerical experiment, Physical Review E 74 (2006) 036305.
[133] V. Ruban, Enhanced rise of rogue waves in slant wave groups, JETP Letters 94 (3) (2011) 177–181.
[134] I.E. Alber, The effects of randomness on the stability of two dimensional surface wave trains, Proceedings of The Royal Society of London. Series A A636 (1978) 525–546.
[135] I.E. Alber, P. Saffman, Stability of random nonlinear deep water waves with finite bandwidth spectra, Techincal Report -TRW Defense and Space System Group, vol. 31326-6035-RU-, 1978.
[136] M. Onorato, A. Osborne, R. Fedele, M. Serio, Landau damping and coherent structures in narrow-banded 1+ 1 deep water gravity waves, Physical Review E 67 (4) (2003) 046305.
[137] A. Regev, Y. Agnon, M. Stiassnie, O. Gramstad, Sea-swell interaction as a mechanism for the generation of freak waves, Physics of Fluids 20 (2008) 112102.
[138] E. Wigner, On the quantum correction for thermodynamic equilibrium, Physical Review 40 (5) (1932) 749.
[139] D. Crawford, P. Saffman, H. Yuen, Evolution of a random inhomogeneous field of nonlinear deep-water gravity waves, Wave Motion 2 (1) (1980) 1–16.
[140] J. Hammack, D. Henderson, H. Segur, Deep-water waves with persistent, two-dimensional surface patterns, Journal of Fluid Mechanics 532 (2005) 1–51.
[141] M. Onorato, A. Osborne, M. Serio, Modulation instability in crossing sea states: a possible mechanism for the formation of freak waves, Physical Review Letters 96 (2006) 014503-4.
[142] P.K. Shukla, I. Kaurakis, B. Eliasson, M. Marklund, L. Stenflo, Instability and evolution of nonlinearly interacting water waves, Physical Review Letters 97 (2006) 094501-4.
[143] G.A. , E.B. , M. Marklund, Evolution of rogue waves in interacting wave systems, EPL 86 (2) (2009) APR.
[144] V. Ruban, Two different kinds of rogue waves in weakly crossing sea states, Physical Review E 79 (6) (2009) 065304.
[145] V. Ruban, Giant waves in weakly crossing sea states, Journal of Experimental and Theoretical Physics 110 (3) (2010) 529–536.
[146] M. Onorato, D. Proment, A. Toffoli, Freak waves in crossing seas, The European Physical Journal-Special Topics 185 (1) (2010) 45–55.
[147] F. Baronio, A. Degasperis, M. Conforti, S. Wabnitz, Solutions of the vector nonlinear Schrödinger equations: evidence for deterministic rogue waves, Physical Review Letters 109 (4) (2012) 44102.
[148] A. Toffoli, E. Bitner-Gregersen, A. Osborne, M. Serio, J. Monbaliu, M. Onorato, Extreme waves in random crossing seas: laboratory experiments and numerical simulations, Geophysical Research Letters 38 (6) (2011) L06605.
[149] L. Cavaleri, L. Bertotti, L. Torrisi, E. Bitner-Gregersen, M. Serio, M. Onorato, Rogue waves in crossing seas: the Louis Majesty accident, Journal of Geophysical Research 117 (2012) C00J10.

[150] H. Tamura, T. Waseda, Y. Miyazawa, Freakish sea state and swell-windsea coupling: numerical study of the suwa-maru incident, Geophysical Research Letters 36 (2009) L01607.
[151] J.K. Mallory, Abnormal waves in the southeast coast of South Africa, International Hydrographic Review 51 (1974) 99–129.
[152] D. Peregrine, Interaction of water waves and currents, Advances in Applied Mechanics 16 (1976) 9–117.
[153] E.J. Heller, L. Kaplan, D.A. , Refraction of a Gaussian seaway, Journal of Geophysical Research 113 (2008) C09023.
[154] I. Lavrenov, The wave energy concentration at the agulhas current of South Africa, Natural Hazard 17 (1998) 117–127.
[155] M. Brown, Space–time surface gravity wave caustics: structurally stable extreme wave events, Wave Motion 33 (2) (2001) 117–143.
[156] M. Brown, The maslov integral representation of slowly varying dispersive wavetrains in inhomogeneous moving media, Wave Motion 32 (3) (2000) 247–266.
[157] K. Dysthe, Refraction of gravity waves by weak current gradients, Journal of Fluid Mechanics 442 (2001) 157–159.
[158] T. Janssen, T. Herbers, Nonlinear wave statistics in a focal zone, Journal of Physical Oceanography 39 (8) (2009) 1948–1964.
[159] K. Hjelmervik, K. Trulsen, Freak wave statistics on collinear currents, Journal of Fluid Mechanics 637 (2009) 267–284.
[160] M. Onorato, D. Proment, A. Toffoli, Triggering rogue waves in opposing currents, Physical Review Letters 107 (18) (2011) 184502.
[161] V. Ruban, Comment on triggering rogue waves in opposing currents, Arxiv preprint arXiv:1110.4710, 2011.
[162] L. Ying, Z. Zhuang, E. Heller, L. Kaplan, Linear and nonlinear rogue wave statistics in the presence of random currents, Nonlinearity 24 (2011) R67.
[163] A.N. Ganshin, V.B. Efimov, G.V. Kolmakov, L.P. Mezhov-Deglin, P.V.E. Mcclintock, Observation of an inverse energy cascade in developed acoustic turbulence in superfluid Helium, Physical Review Letters 101 (2008) 065303.
[164] R. Höhmann, U. Kuhl, H.-J. Stöckmann, L. Kaplan, E.J. Heller, Freak waves in the linear regime: a microwave study, Physical Review Letters 104 (9) (2010) 093901.
[165] M. Shats, H. Punzmann, X.H. , Capillary rogue waves, Physical Review Letters 104 (2010) 104503.
[166] W.M. Moslem, R. Sabry, S.K. El-Labany, P.K. Shukla, Dust-acoustic rogue waves in a nonextensive plasma, Physical Review E 84 (6) (2011) 066402.
[167] D. Laveder, T.T. Passot, P. Sulem, G. Sánchez-Arriaga, Rogue waves in Alfvénic turbulence, Physics Letters A 375 (2011) 3997–4002.
[168] Y. Bludov, V. Konotop, N. Akhmediev, Matter rogue waves, Physical Review A 80 (3) (2009) 33610.
[169] A. Maluckov, L. Hadzievski, N. Lazarides, G.P. Tsironis, Extreme events in discrete nonlinear lattices, Physical Review E 79 (2, Part 2) (2009).
[170] V.B. Efimov, A.N. Ganshin, G.V. Kolmakov, P.V.E. Mcclintock, L.P. Mezhov-Deglin, Rogue waves in superfluid Helium, European Physical Journal - Special Topics 185 (2010) 181–183.
[171] M. Faraday, On the forms and states assumed by fluids in contact with vibrating elastic surfaces, Philosophical Transactions of the Royal Society of London 121 (1831) 319.
[172] G. Nicolis, C. Nicolis, Foundations of Complex Systems: Nonlinear Dynamics, Statistical Physics, Information and Prediction, World Scientific, 2007.
[173] J.M. Dudley, G. Genty, S. Coen, Supercontinuum generation in photonic crystal fiber, Reviews of Modern Physics 78 (4) (2006) 1135–1184.
[174] N. Akhmediev, J. Soto-Crespo, A. Ankiewicz, Extreme waves that appear from nowhere: on the nature of rogue waves, Physics Letters A 373 (25) (2009) 2137–2145.
[175] A. Mussot, A. Kudlinski, M. Kolobov, E. Louvergneaux, M. Douay, M. Taki, Observation of extreme temporal events in CW-pumped supercontinuum, Optics Express 17 (19) (2009) 17010–17015.
[176] M. Taki, A. Mussot, A. Kudlinski, E. Louvergneaux, M. Kolobov, M. Douay, Third-order dispersion for generating optical rogue solitons, Physics Letters A 374 (4) (2010) 691–695.
[177] M. Erkintalo, G. Genty, J.M. Dudley, Rogue-wave-like characteristics in femtosecond supercontinuum generation, Optics Letters 34 (16) (2009) 2468–2470.
[178] K. Hammani, C. Finot, J.M. Dudley, G. Millot, Optical rogue-wave-like extreme value fluctuations in fiber Raman amplifiers, Optics Express 16 (21) (2008) 16467–16474.
[179] V. Zakharov, V. Lvov, G. Falkovich, Kolmogorov Spectra of Turbulence I: Wave Turbulence, Springer, 1992.
[180] U. Bortolozzo, J. Laurie, S. Nazarenko, S. Residori, Optical wave turbulence and the condensation of light, Journal of the Optical Society of America B 26 (12) (2009) 2280–2284.
[181] J. Laurie, U. Bortolozzo, S. Nazarenko, S. Residori, One-dimensional optical wave turbulence: experiment and theory, Physics Report (2012).
[182] A.I.D. Dyachenko, V.E. Zakharov, A.N. Pushkarev, V.F. Shvets, V.V. Yankov, Soliton turbulence in nonintegrablewave systems, Soviet Physics JETP 69 (1989) 1144–1147.
[183] C. Bonatto, M. Feyereisen, S. Barland, M. Giudici, C. Masoller, J. Leite, J. Tredicce, Deterministic optical rogue waves, Physical Review Letters 107 (5) (2011) 153901.
[184] A. Pisarchik, R. Jaimes-Reátegui, R. Sevilla-Escoboza, G. Huerta-Cuellar, M. Taki, Rogue waves in a multistable system, Physical Review Letters 107 (27) (2011) 1–5.
[185] M. Erkintalo, G. Genty, J.M. Dudley, On the statistical interpretation of optical rogue waves, European Physical Journal - Special Topics 16 (185) (2010) 135–144.
[186] S. Vergeles, S.K. Turitsyn, Optical rogue waves in telecommunication data streams, Physical Review A 83 (6) (2011) 061801.
[187] D.V. Churkin, O.A. Gorbunov, S.V. Smirnov, Extreme value statistics in Raman fiber lasers, Optics Letters 36 (18) (2011) 3617–3619.
[188] J.M. Soto-Crespo, P. Grelu, N. Akhmediev, Dissipative rogue waves: extreme pulses generated by passively mode-locked lasers, Physical Review E 84 (1) (2011) 1–7.
[189] R.J. Boggavarapu, J. Grantham, Y.Z. Hu, F. Brown de colstoun, C.W. Lowry, G. Khitrova, S.W. Koch, M. Sargent im, G.H.M. , Instabilities of a microcavity laser with a weak injected signal, Optics Letters 18 (21) (1993) 1846–1848.
[190] M. San miguel, R. Toral, Stochastic effects in physical systems, in: E. Tirapegui, W. Zeller (Eds.), Instabilities and Nonequilibrium Structures, VI, Kluwer, 1997, pp. 609–612.
[191] J. Kasparian, P. Bejot, J.P. Wolf, J.M. Dudley, Optical rogue wave statistics in laser filamentation, Optics Express 17 (14) (2009) 12 070–12 075.
[192] D. Majus, V. Jukna, G. Valiulis, D. Faccio, A. Dubietis, Spatiotemporal rogue events in femtosecond filamentation, Physical Review A 83 (2) (2011) 2–5.
[193] D. Majus, V. Jukna, E. Pileckis, G. Valiulis, A. Dubietis, Spatiotemporal rogue events in femtosecond filamentation, Optics Express 19 (17) (2011) 16 317–16 323.
[194] U. Bortolozzo, A. Montina, F.T. Arecchi, J.P. Huignard, S. Residori, Spatiotemporal pulses in a liquid crystal optical oscillator, Physical Review Letters 99 (2) (2007) 3–6.
[195] P. Aubourg, J.P. Huignard, M. Hareng, R.A. Mullen, Liquid crystal light valve using bulk monocrystalline $Bi_{12}SiO_{20}$ as the photoconductive material, Applied Optics 21 (20) (1982) 3706–3712.
[196] U. Bortolozzo, S. Residori, A. Petrosyan, J.P. Huignard, Pattern formation and direct measurement of the spatial resolution in a photorefractive liquid crystal light valve, Optical Communications 263 (2006) 317–321.
[197] A.E. Siegman, Lasers, Oxford University Press, Oxford, 1986.
[198] P.D. Gennes, J. Prost, The Physics of Liquid Crystals, Oxford Science Publications, 1992.
[199] A. Montina, U. Bortolozzo, S. Residori, J.P. Huignard, F. Arecchi, Complex dynamics of a unidirectional optical oscillator based on a liquid-crystal gain medium, Physical Review A 76 (3) (2007) 1–14.
[200] S. Residori, U. Bortolozzo, A. Montina, F. Lenzini, F.T. Arecchi, Rogue waves in spatially extended optical systems, Fluctuations and Noise Letters (2012).
[201] J.W. Goodman, Speckle Phenomena in Optics: Theory and Applications, Roberts and Company Publishers, Greenwood Village, CO 80111, USA, 2007.
[202] P. Sibani, P. Littlewood, Slow dynamics from noise adaptation, Physical Review Letters 71 (1993) 1482–1485.
[203] T.O. Richardson, E.J.H. Robinson, K. Christensen, H.J. Jensen, N.R. Franks, A.B. Sendova-Franks, Record dynamics in ants, PLoS ONE 5 (3) (2010) e9621.